Geophysical Journal International

Geophys. J. Int. (2013) **194,** 125–144
Advance Access publication 2013 April 23

doi: 10.1093/gji/ggt117

Analyses of marginal stability, heat transfer and boundary layer properties for thermal convection in a compressible fluid with infinite Prandtl number

Xi Liu and Shijie Zhong

Department of Physics, University of Colorado, Boulder, CO 80309*, USA. E-mail: xi.liu@colorado.edu*

Accepted 2013 March 20. Received 2013 March 12; in original form 2012 July 16

SUMMARY

Thermal and dynamical evolution of planets is controlled by thermal convection in planetary mantles. Mantle compressibility, which measures volume change due to pressure change and its associated energetic effects, can have important effects on planetary mantle convection. However, key issues including marginal stability analysis, thermal boundary properties and heat transfer in compressible mantle convection are not well understood. This paper studies the influence of mantle compressibility on thermal convection in an isoviscous and compressible fluid with infinite Prandtl number, using both marginal stability analysis and numerical modelling. For the marginal stability analysis, a new formulation of the propagator matrix method is implemented to compute the critical Rayleigh number Ra_c and the corresponding eigenfunctions for compressible convection at different wavelengths (i.e. wavenumber k_x) and dissipation number Di which measures the compressibility. Ra_c from the analysis is in a good agreement with that determined from the numerical experiment using the eigenfunctions as initial perturbations. Our study suggests that if Ra is defined by the surface density, the minimum Ra_c may occur at non-zero Di. Finite element models are computed for compressible mantle convection at different Ra and Di. Heat flux and thermal boundary layer (TBL) properties including boundary layer thickness and temperature difference are quantified and analysed from the numerical results. Scaling laws of temperature differences across TBLs and of the heat flux are derived analytically for compressible mantle convection and are verified by the numerical results. This study shows that while TBL thicknesses and the heat flux are still scaled with Ra to the $-1/3$ and $1/3$ power, respectively, as those for incompressible convection, they also strongly depend on Di. In particular, compressibility breaks the symmetry for the top and bottom TBLs, and the ratios of thickness and temperature difference for the top TBL to those for the bottom TBL are $exp(Di/2)$. These results have important implications for compressible mantle convection.

Key words: Instability analysis; Heat flow; Mantle processes; Dynamics of lithosphere and mantle.

1 INTRODUCTION

Thermal convection within planetary mantles controls thermal and dynamic evolution of planets. Most studies on Earth's mantle convection employ a Boussinesq approximation that assumes an incompressible mantle. Classic studies with the Boussinesq approximation provide an important understanding of Earth's mantle convection and interior dynamics (e.g. McKenzie *et al.* 1974). However, by formulating compressible mantle convection models, a number of studies have also examined the non-Boussinesq effects including depth-dependent density, viscous heating and adiabatic heating (e.g. Jarvis & McKenzie 1980; Steinbach *et al.* 1989).

In their classic work on compressible mantle convection, Jarvis & McKenzie (1980) formulated a 2-D Cartesian model and systematically investigated the marginal stability problem and finite amplitude convection. Other models of compressible convection have been formulated to examine the effects of equations of state (Ita & King 1994), variable viscosity (Tackley 1996), spherical geometry (Bercovici *et al.* 1992) and dynamic pressure in the buoyancy term (Leng & Zhong 2008a). Recently, Tan *et al.* (2011) incorporated variable viscosity and material properties into 3-D spherical models of compressible mantle convection. Also, a number of studies showed that mantle compressibility has significant effects on plume dynamics. It has been demonstrated that the number of plumes is reduced in compressible convection since small-scale plumes merge to form super-plumes (Balachandar *et al.* 1992; Thompson & Tackley 1998; Tan & Gurnis 2005). Leng & Zhong (2008b) reported that the compressibility has a controlling effect on plume excess

temperature and plume heat flux. Tan *et al.* (2011) found that in a compressible mantle, the plumes form around the edges of chemical 'domes' at the core mantle boundary.

However, more studies are needed to better understand the marginal stability analysis and scaling laws of convective heat flux for compressible mantle convection. Marginal stability analysis was performed for compressible convection with limited parameters and restricted boundary conditions (Jarvis & McKenzie 1980; Bercovici *et al.* 1992). While scaling laws of heat flux and thermal boundary layer (TBL) properties are well understood for Cartesian incompressible thermal convection, they remain poorly understood for compressible convection. Recently, as more exoplanets or super-Earths are detected (e.g. Charbonneau *et al.* 2009), there is a growing interest in understanding the mantle dynamics for these planets (e.g. O'Neill & Lenardic 2007; Valencia *et al.* 2007; Van Heck & Tackley 2011; Foley *et al.* 2012). A distinct character of super-Earths' mantles is their very large compressibility and Rayleigh number, due to their sizes and masses. Most of previous studies on compressible mantle convection considered compressibility in a range appropriate to Earth, and now it is necessary to consider larger compressibility.

In this study, we perform marginal linear stability analysis using a new technique based on a propagator matrix method. We also compute finite amplitude compressible models with a wide range of mantle compressibility and Rayleigh number, and derive scaling laws for TBL properties and convective heat transfer. In the following section, we present model formulation and governing equations. In Section 3, we show results for the marginal stability analysis of compressible convection. In Section 4, we present finite amplitude convection calculations and derive scaling laws for TBL properties and heat flux. In Sections 5 and 6, we discuss the implications of our results for compressible convection and make concluding remarks.

2 MODEL FORMULATION

2-D Cartesian models are formulated with an anelastic-liquid approximation (ALA) (e.g. Jarvis & McKenzie 1980; Schubert *et al.* 2001). ALA uses depth-dependent parameters, notably density $\rho_r(z)$ as reference state in the governing equations. In this study, parameters such as viscosity, thermal conductivity, specific heat and thermal expansion are assumed constant in our models unless otherwise indicated.

$\rho_r(z)$ is determined by the Adams–Williamson equation of state by Birch (1952):

$$\frac{1}{\rho_r}\frac{\mathrm{d}\rho_r}{\mathrm{d}z} = -\frac{\alpha g}{c_P \Gamma}, \tag{1}$$

where z is the vertical coordinate pointing upwards, g is the gravitational acceleration, α is the coefficient of thermal expansion, c_P is the specific heat at constant hydrostatic pressure and Γ is the Grüneisen's parameter and is defined as

$$\Gamma = \frac{\alpha \mathrm{K}_S}{\rho c_P}, \tag{2}$$

where K_S is the isentropic bulk modulus. Note that in our model with homogeneous composition, isentropic and adiabatic process may be viewed as equivalent. We also assume that Γ is constant.

In ALA, the density anomaly $\Delta\rho$ is determined by both temperature perturbation $T' = T - T_r$ and dynamic pressure p,

$$\Delta\rho = \rho_r \left[-\alpha (T - T_r) + \mathrm{K}_T^{-1} p\right], \tag{3}$$

where T_r is the reference temperature and K_T is the isothermal bulk modulus. In our models, we make assumption that $\mathrm{K}_T \approx \mathrm{K}_S$, which simplifies the compressible mantle convection problem as discussed in Schubert *et al.* (2001).

With assumption of infinite Prandtl number, the conservation equations of mass, momentum and energy can be written as follows (Jarvis & McKenzie 1980; Ita & King 1994; Leng & Zhong 2008a; King *et al.* 2010):

$$(\rho_r u_i)_{,i} = 0, \tag{4}$$

$$-p_{,j}\delta_{ij} + \tau_{ij,j} - \Delta\rho g \delta_{iz} = 0, \tag{5}$$

$$\rho_r c_P \dot{T} + \rho_r c_P u_i T_{,i} + \rho_r g \alpha T u_z = (kT_{,i})_{,i} + \tau_{ij} u_{i,j} + \rho_r H, \tag{6}$$

where u_i and T are the velocity vector and temperature, τ is the deviatoric stress tensor, $\dot{T}$ is the derivative of temperature with respect to time t, k is the thermal conductivity, H is the heat production rate, i and j are spatial indices and z means vertical direction and δ_{ij} is the Kronecker delta function.

The deviatoric stress tensor τ_{ij} is determined by a rheology equation

$$\tau_{ij} = \eta\left(\frac{\partial u_i}{\partial x_j} + \frac{\partial u_j}{\partial x_i} - \frac{2}{3}\delta_{ij}\frac{\partial u_k}{\partial x_k}\right), \tag{7}$$

where η is the viscosity.

Eqs (4)–(6) can be non-dimensionalized with the following characteristic values:

$$x_i = d x_i', \quad u_i = \frac{\kappa_0}{d} u_i', \quad T = \Delta T T' + T_s, \quad T_s = \Delta T T_s',$$
$$\rho_r = \rho_0 \rho_r', \quad t = \frac{d^2}{\kappa_0} t', \quad H = \frac{H' \kappa_0 \Delta T c_{P0}}{d^2}, \quad \eta = \eta_0 \eta',$$
$$p = \frac{\eta_0 \kappa_0}{d^2} p', \quad \alpha = \alpha_0 \alpha', \quad g = g_0 g', \quad c_P = c_{P0} c_P',$$
$$\Gamma = \Gamma_0 \Gamma', \quad k = k_0 k', \tag{8}$$

where symbols with primes are dimensionless; symbols with a subscript 0 are surface values of corresponding parameters and are used as the reference to scale the dimensional variables; d is the mantle thickness, ΔT is the total temperature difference across the layer and T_s is the surface temperature which is taken as 273K in this study; κ_0 is the reference thermal diffusivity and is defined as $\kappa_0 = k_0/(\rho_0 c_{P0})$.

After dropping the primes, the dimensionless governing equations for ALA are as follows (e.g. Leng & Zhong 2008a):

$$(\rho_r u_i)_{,i} = 0, \tag{9}$$

$$-p_{,j}\delta_{ij} + \tau_{ij,j} + [\rho_r \alpha g Ra (T - T_r) - \frac{\alpha g}{c_P \Gamma} p\gamma]\delta_{iz} = 0, \tag{10}$$

$$\rho_r c_P \dot{T} + \rho_r c_P u_i T_{,i} + \rho_r Di \alpha g u_z (T + T_s) = (kT_{,i})_{,i} + \frac{Di}{Ra}\tau_{ij} u_{i,j} + \rho_r H, \tag{11}$$

where Ra is the Rayleigh number, Di is the dissipation number and γ is the mantle compressibility. They are defined as

$$Ra = \frac{\rho_0^2 c_{P0} \alpha_0 g_0 \Delta T d^3}{k_0 \eta_0}, \tag{12}$$

$$Di = \frac{\alpha_0 g_0 d}{c_{P0}}, \tag{13}$$

$$\gamma = \frac{Di}{\Gamma_0}. \tag{14}$$

In our model, Γ_0 is taken as 1; therefore, $Di = \gamma$. The dimensionless surface temperature T_s is fixed as 0.091 and the heat production rate H in eq. (11) is zero. The non-dimensional values of Γ, α, k, g and c_P are all 1 in eqs (9)–(11) unless otherwise indicated.

The dimensionless Adams–Williamson equation is

$$\frac{1}{\rho_r}\frac{\mathrm{d}\rho_r}{\mathrm{d}z} = -\frac{\alpha g}{c_p \Gamma}\gamma. \tag{15}$$

With $\alpha g/(c_P\Gamma) = 1$ and $Di = \gamma$, the dimensionless reference density profile is

$$\rho_r(z) = \rho_0 e^{Di(1-z)}. \tag{16}$$

We consider 2-D Cartesian models within a box of non-dimensional height of 1 and length L. The top and bottom boundaries are set as $z = 1$ and $z = 0$, respectively. We use free-slip boundaries with zero normal velocities and tangential stresses at the four boundaries of the box. The non-dimensional temperature is fixed at 0 and 1 on the top and bottom boundaries, respectively, and the sidewalls are thermally insulated.

Two different analyses are presented in this study: the marginal stability analysis and the finite amplitude convection calculations. We use the finite element code developed by Leng & Zhong (2008a) for numerical experiments of compressible mantle convection. This code is based on incompressible mantle convection code Citcom (Moresi *et al.* 1996) and has been benchmarked (Leng & Zhong 2008a; King *et al.* 2010).

3 MARGINAL LINEAR STABILITY ANALYSIS USING PROPAGATOR MATRIX METHOD

Rayleigh number, Ra, is an important non-dimensional number that determines the vigour of convection. Convection occurs when Ra exceeds a critical value Ra_c. Marginal linear stability analysis can be used to study the onset of mantle convection and to determine Ra_c (e.g. Jeffreys 1930; Turcotte & Schubert 2002). Classic analyses using a stream-function formulation have been used to determine Ra_c for incompressible fluid with uniform thermodynamic parameters and the same boundary conditions as our models (e.g. Turcotte & Schubert 2002) and Ra_c is:

$$Ra_c = \frac{(\pi^2 + \mathrm{k}_x^2)^3}{\mathrm{k}_x^2}, \tag{17}$$

where k_x is the wavenumber of horizontal perturbation.

For compressible convection with depth-dependent density and possibly other depth-dependent thermodynamic properties, propagator matrix method is more effective. The propagator matrix method has been used to obtain analytic solution of the Stokes flow problem for incompressible (Hager & O'Connell 1981) and compressible (Leng & Zhong 2008a) models. With a stream-function and vorticity formulation, Jarvis & McKenzie (1980) employed the propagator matrix method for marginal stability analysis with heat flux boundary conditions. Buffet *et al.* (1994) used the propagator matrix method for marginal stability analysis for incompressible flows with depth-dependent viscosity. In this study, we develop a new implementation of propagator matrix method for marginal stability analysis for both incompressible and compressible flows with free-slip and isothermal boundary conditions. Our implementation is based on a stress–velocity formulation which is similar to that in Leng & Zhong (2008a), but we also incorporate the linearized energy equation. The setup of propagator matrix and the solution procedure are discussed in Appendix A. In the following sections, we will outline the basic principles of marginal stability analysis and present the critical Rayleigh number of compressible convection as well as the corresponding eigenfunctions solved by the propagator matrix method.

3.1 Linearized governing equations

Marginal linear stability analysis is performed in the limit of weak convection, in which the governing equations can be linearized around a background state (Turcotte & Schubert 2002). For basal heating convection with a fixed temperature of 1 at the bottom and 0 at the top, and with constant thermal conductivity, the reference temperature is set to be $T_r = 1 - z$, that is, purely conductive temperature. Introduce a small perturbation T' into reference temperature, such that $T = T_r + T'$, and the perturbed temperature leads to non-zero horizontal and vertical velocities $u'$and v', as well as non-zero shear and normal stresses $\tau'$and σ'.

Since T', u', v', τ' and σ' are all of small magnitude, the governing eqs (9)–(11) can be linearized as follows:

$$\left(\rho_r u_i'\right)_{,i} = 0, \tag{18}$$

$$-p_{,j}\delta_{ij} + \tau'_{ij,j} + \left(\rho_r \alpha g Ra T' - \frac{\alpha g}{c_P \Gamma} p Di\right)\delta_{i3} = 0, \tag{19}$$

$$\rho_r c_P \dot{T}' - \rho_r c_P v' + \rho_r \alpha g v' Di(1 - z + T_s) = k\nabla^2 T'. \tag{20}$$

The dependences of the perturbations on x and z are separable. The horizontal and vertical components of the perturbations are represented by sinusoidal functions and arbitrary functions, respectively. Take the temperature perturbation T' as an example, T' can be expressed in Fourier transform as

$$T' = \int T_0(z)\sin(\mathrm{k}_x x)e^{\alpha' t}\mathrm{d}\mathrm{k}_x, \tag{21}$$

where k_x is the wavenumber of the horizontal component of temperature perturbation, $T_0(z)$ is the vertical dependence of the temperature perturbation, and α' is the growth rate and is taken as a real number. Note that both $T_0(z)$ and α' in eq. (21) are corresponding to k_x. Perturbations should satisfy the boundary conditions. The isothermal boundary condition in our model requires that $T'(z = 0) = T'(z = 1) = 0$ and $T_0(z)$ in eq. (21) should be 0 at $z = 0$ and $z = 1$. The critical Rayleigh number, Ra_c, is determined as the value of Ra at $\alpha' = 0$. $T_0(z)$ at $\alpha' = 0$ is the eigenfunction of temperature perturbation for corresponding Ra_c, that is, the corresponding k_x and Di.

The other four perturbations, u', v', τ' and σ', are expressed in similar forms to that of T' in Appendix A. The vertical dependences of u', v', $\tau'$and σ' are denoted as $U(z)$, $V(z)$, $Y_{xz}(z)$ and $S_{zz}(z)$, respectively.

In Appendix A, we discuss that with a stress–velocity formulation, the linearized governing eqs (18)–(20) for a compressible fluid can be written as a vector linear differential equation:

$$\frac{\mathrm{dW}}{\mathrm{d}z} = \mathrm{AW}, \tag{22}$$

where A is a 6×6 matrix consisting of Ra, Di, k_x, and other parameters, and W is a 6×1 vector:

$$\mathrm{W} = \left(V, U, \frac{S_{zz}}{2\mathrm{k}_x}, \frac{Y_{xz}}{2\mathrm{k}_x}, T_0, \frac{\mathrm{d}T_0}{\mathrm{d}z} \right)^{\mathrm{T}}, \tag{23}$$

where superscript T denotes the matrix transpose.

The solution approach to eq. (22) using the propagator matrix method and calculations of critical Rayleigh number and the corresponding eigenfunctions are described in Appendix A.

This implementation of propagator matrix method is general and can be used for marginal stability analysis for both incompressible and compressible media with either homogeneous or depth-dependent thermodynamic and material properties such as thermal conductivity or viscosity.

3.2 Results for Ra_c and eigenfunctions

We first show calculations of Ra_c for incompressible ($Di = 0$) and homogeneous fluid at fundamental mode $n = 0$ from our method. Here mode n represents the number of internal nodes of the vertical velocity eigenfunction, $V(z)$ (i.e. the first mode or $n = 1$ mode has one $V(z) = 0$ node, and thus two cells in the vertical direction). We use 129 uniform grid points in z direction to compute propagator matrix for all the results shown in this study. Fig. 1(a) shows Ra_c for different wavenumbers k_x and the results are identical to those from classic analysis given by eq. (17).

For compressible fluid, Ra_c at fundamental mode $n = 0$ and first mode $n = 1$ are determined and given in Table 1 and Figs 1(b) and (c). We determined Ra_c at $n = 0$ mode for $Di = 0$, 0.5, 1 and 1.5, and k_x from 0.1π to 3π. We found that $n = 0$ mode does not exist for large Di. For example, for $k_x = 0.5\pi$, π and 2π, the maximum Di with which $n = 0$ mode exists is 1.9, 1.8 and 1.7, respectively. We also determined Ra_c at $n = 1$ mode for $Di = 0$, 0.5, 1 and 2, and k_x varying from 0.5π to 2π. Ra_c for $n = 1$ mode is much larger than that for $n = 0$ mode. It is expected that $n = 1$ mode does not exist for even larger Di (e.g. Jarvis & McKenzie 1980), but we did not explore this topic further.

We now examine the dependence of Ra_c on dissipation number Di and wavenumber k_x. At the fundamental mode ($n = 0$), curves of Ra_c versus k_x for $Di = 0$ and $Di = 1$ are nearly identical, and are both higher than Ra_c for $Di = 0.5$ (Fig. 1b). As Di increases from 1 to 1.5, Ra_c increases rapidly. For a particular wavenumber $k_x = \pi$ and mode $n = 0$ (Fig. 1d), while Ra_c increases rapidly with Di at large Di ($Di > 1$), following an approximately exponential function of Di, Ra_c decreases with Di from $Di = 0$ to $Di = 0.6$. However, if Ra is defined by the averaged density $\bar{\rho}$, where $\bar{\rho} = \int_0^1 \rho_r(z)\mathrm{d}z = \rho_0(e^{Di} - 1)/Di$, rather than the surface density ρ_0 as in eq. (12), Ra_c would increase monotonically with Di (Fig. 1d). Ra_c shows similar Di dependences for wavenumbers $k_x = 0.5\pi$ and $k_x = 2\pi$ at fundamental mode (Table 1). For $n = 1$ mode, Ra_c increases with Di for Di varying from 0 to 1 (Fig. 1c). While for $n = 0$ mode, the wavenumber k_x at which Ra_c is minimum is about $\sqrt{2}\pi/2$

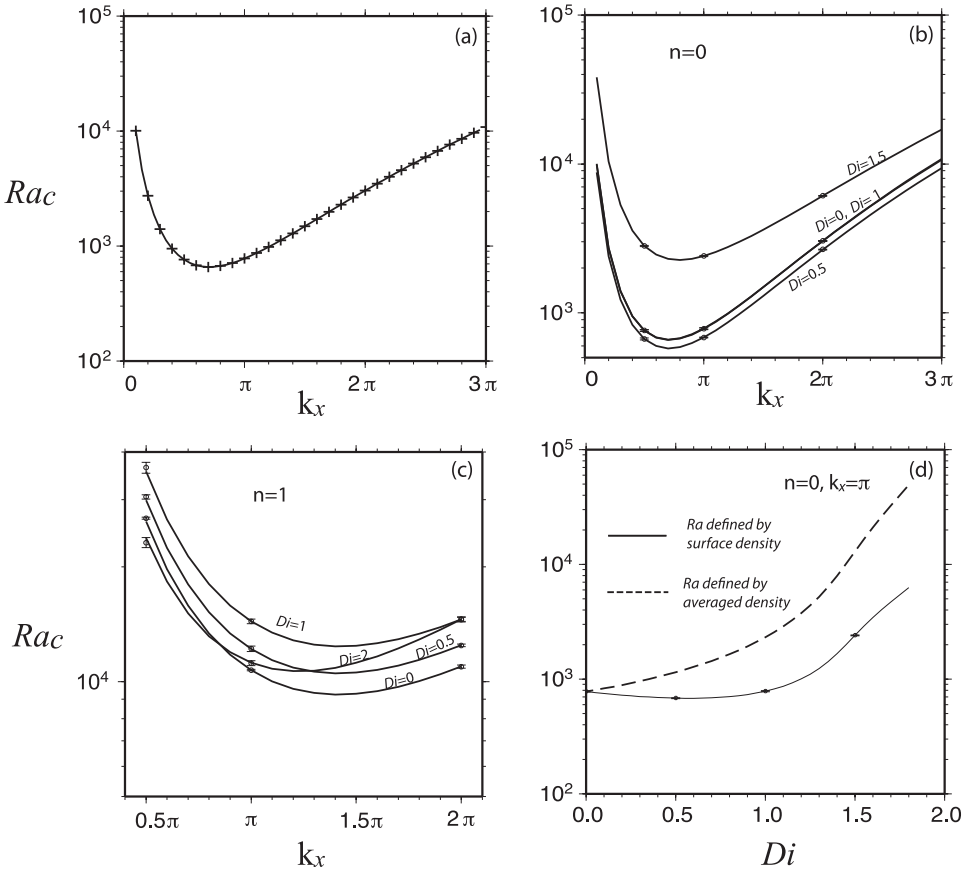

Figure 1. (a) Critical Rayleigh number Ra_c versus wavenumber k_x for incompressible fluid with uniform thermodynamic parameters and fixed temperature boundary conditions. The '+' symbols represent Ra_c from propagator matrix method and the line represents Ra_c from eq. (17). (b) and (c) Ra_c versus k_x for compressible fluid with uniform thermodynamic parameters at (b) fundamental mode $n = 0$ and for different Di; (c) first higher mode $n = 1$ and for different Di. (d) Ra_c versus Di at $k_x = \pi$ for $n = 0$. In (b), (c) and (d), the lines are Ra_c (defined by surface density) from the marginal stability analysis, and the circles are those from numerical experiments with error bars (Table 1). In (d), the dashed line represents Ra_c defined by depth-averaged density.

Table 1. Critical Rayleigh number computed by propagator matrix method (analytical) and finite element modelling (numerical).

Mode n	Wave number k_x (π)	Di	Ra_c (analytical)	averaged Ra_c (numerical)	Error
0	0.5	0	761	760	±0.8 per cent
0	0.5	0.5	667	667	±0.7 per cent
0	0.5	1	761	760	±0.8 per cent
0	0.5	1.5	2812	2812	±0.5 per cent
0	1	0	779	779	±0.8 per cent
0	1	0.5	683	683	±0.4 per cent
0	1	1	785	785	±0.6 per cent
0	1	1.5	2408	2408	±0.5 per cent
0	2	0	3044	3045	±0.2 per cent
0	2	0.5	2652	2645	±0.5 per cent
0	2	1	3035	3035	±0.3 per cent
0	2	1.5	6101	6100	±0.3 per cent
1	0.5	0	29 910	30 500	±0.7 per cent
1	0.5	0.5	26 321	26 825	±0.3 per cent
1	0.5	1	35 533	36 400	±1.6 per cent
1	0.5	2	23 775	23 150	±1.5 per cent
1	1	0	12 176	12 200	±0.8 per cent
1	1	0.5	10 714	10 725	±0.2 per cent
1	1	1	14 394	14 400	±0.7 per cent
1	1	2	11 215	11 180	±0.7 per cent
1	2	0	12 468	12 450	±0.4 per cent
1	2	0.5	10 963	10 950	±0.5 per cent
1	2	1	14 557	14 550	±0.7 per cent
1	2	2	14 572	14 600	±0.7 per cent

for $Di \leq 1$, this critical wavenumber increases with Di (Fig. 1b), suggesting that smaller convective wavelength is favoured for larger Di.

The eigenfunctions $T_0(z)$, $U(z)$ and $V(z)$ are shown in Fig. 2. It is found that compressibility, or Di, has a significant effect on these eigenfunctions (Figs 2a and b). For $Di = 0$, $T_0(z)$, $U(z)$ and $V(z)$ are purely sinusoidal functions (Fig. 2, plotted in dashed lines as references for other cases). For $Di = 1$, $T_0(z)$, $U(z)$ and $V(z)$ are similar to sinusoidal functions, but are distorted to have larger amplitudes at shallow depths (or $z > 0.5$) than sinusoidal functions (Fig. 2a). For $Di = 2$, the fundamental mode does not exist, and eigenfunctions of $n = 1$ mode is plotted. It can be seen that $T_0(z)$, $U(z)$ and $V(z)$ differ significantly from sinusoidal functions with flow velocity much stronger at the shallow depths (Fig. 2b). Eigenfunctions are also influenced by depth-dependent thermodynamic parameters (Figs 2c–d).

Ra_c is also determined from numerical experiments for $k_x = 0.5\pi$, π and 2π, with $Di = 0$, 0.5, 1 and 1.5 for the fundamental mode, and $Di = 0$, 0.5, 1, 1.5 and 2 for the first mode, using the finite element code for compressible convection (Leng & Zhong 2008a). We determine the critical Rayleigh number numerically by searching for a Rayleigh number at which the kinetic energy E_k remains constant with time for a given initial perturbation in temperature (Zhong & Gurnis 1993). The initial perturbation is given as

$$T' = cT_0(z)\cos(k_x x), \tag{24}$$

where c is a small number (e.g. 10^{-2}) and $T_0(z)$ is the corresponding eigenfunction determined from the marginal stability analysis for the given Di and k_x as discussed earlier. The kinetic energy E_k of the flow from the numerical models is defined as

$$E_k = \int_S (u^2 + v^2) dS, \tag{25}$$

where the integration domain S represents the whole flow field in the 2-D model. For the given Di and k_x, we calculate E_k for the first 200 time steps and adjust Ra in the model until E_k neither increases nor decays with time (Fig. 3 for E_k versus time for two example cases). The resulting Ra is the critical Rayleigh number where the growth rate is 0 (e.g. Zhong & Gurnis 1993).

Our finite element models use the same model parameters and boundary conditions as those for linear stability analysis. The models use $n_x \times n_z = 257 \times 129$, 129×129 and 65×129 grid points for $k_x = 0.5\pi$, π and 2π, respectively (i.e. the aspect ratio of the box is 2, 1 and 0.5, respectively). Such numerically determined Ra_c for different Di and k_x are in excellent agreement with those from our propagator matrix method with relative difference of less than 1 per cent (Figs 1b–d and Table 1), providing confirmation for both our propagator matrix method and the finite element method for determining Ra_c.

We make two remarks about the eigenfunctions. First, it is well known that for incompressible ($Di = 0$) and homogeneous fluid, the eigenfunctions are sinusoidal functions (e.g. Turcotte & Schubert 2002). We showed that the eigenfunctions are no longer sinusoidal functions for compressible fluid with $Di \neq 0$ and depth-dependent density (Figs 2a and b). Even for incompressible fluid with $Di = 0$, depth-dependent thermal conductivity or thermal expansion also leads to non-sinusoidal forms of eigenfunctions (Figs 2c and d). Second, it is important to use the eigenfunctions of $T_0(z)$ in eq. (24) to determine Ra_c numerically. Although numerical methods have been used to determine Ra_c (e.g. Zhong & Gurnis 1993), it has not been explicitly demonstrated that the eigenfunctions of $T_0(z)$ are needed as initial temperature perturbations. We found that for $Di \neq 0$, if $\sin(\pi z)$ rather than eigenfunction of $T_0(z)$ is used for the initial perturbations, the kinetic energy E_k does not vary monotonically with time and Ra_c cannot be determined accurately.

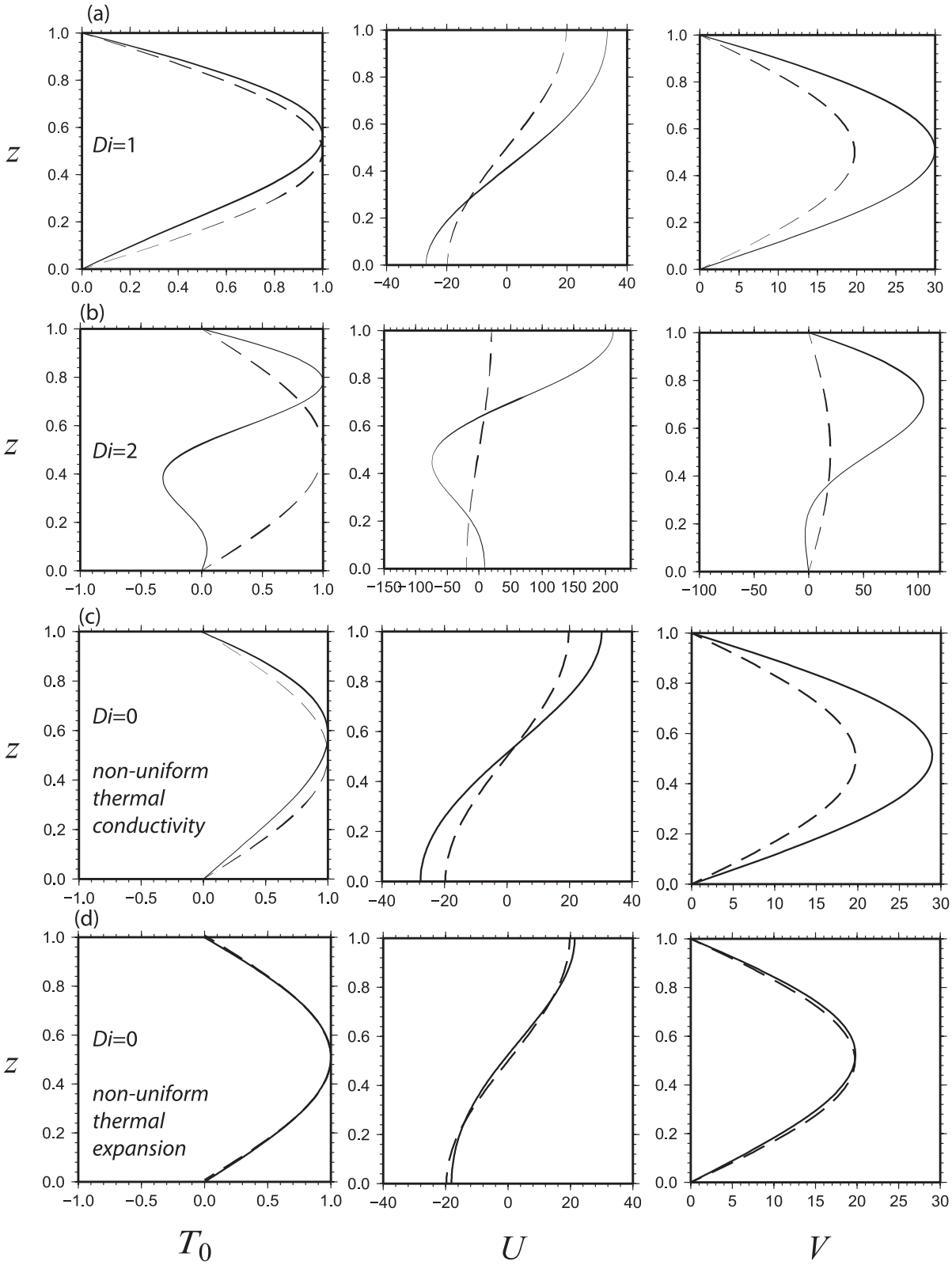

Figure 2. The solid lines are eigenfunctions of temperature (left panel), horizontal velocity (middle panel) and vertical velocity (right panel) for models with non-uniform properties: (a) $Di = 1$; (b) $Di = 2$; (c) non-uniform thermal conductivity that increases linearly from 1 at the top to 2 at the bottom, $Di = 0$; (d) non-uniform thermal expansion that decreases linearly from 1 at the top to 0.2 at the bottom, $Di = 0$. The dashed lines in those figures are the corresponding eigenfunctions for a case with $Di = 0$ and homogeneous fluid and are sinusoidal functions.

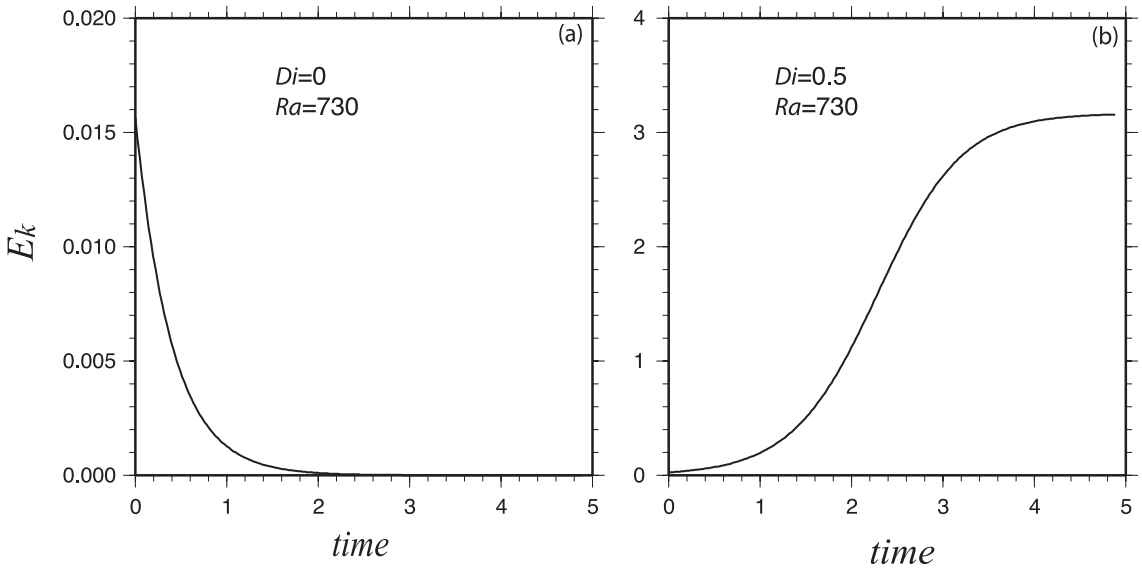

Figure 3. Kinetic energy E_k versus time from numerical calculations using Citcom with $k_x = \pi$, $Ra = 730$ and (a) $Di = 0$; (b) $Di = 0.5$. The critical Rayleigh numbers Ra_c computed from propagator matrix method for these two cases are 779 and 683, respectively. These two calculations show that E_k increases/decreases with time when Ra is greater/less than Ra_c. These two cases were computed for 40 000 time steps (elapsed time ∼5) to reach nearly steady states. For calculations numerically determining Ra_c, models are often computed for 200 time steps.

4 FINITE AMPLITUDE CONVECTION

We computed 2-D Cartesian models of compressible mantle convection at different Ra and Di (Table 2) using a finite element code (Leng & Zhong 2008a). In this study of finite amplitude convection, the models are all 1×1 boxes. All the cases are for basal heating convection with no internal heating. The calculations are done with adequate resolution that produces less than 3 per cent discrepancy between top and bottom heat flux for most cases (Table 2). For all cases, there are at least three elements across a TBL. For most cases with relatively low Ra, calculations start from initial temperature perturbation as in eq. (24). But for cases with high Ra, we choose steady-state temperature field from calculations with either lower resolution or lower Ra as initial conditions. The calculations are run until steady states, or quasi-steady states are attained when averaged heat flux does not change with time (Fig. 4). Compressible convection is more time-dependent in general, as discussed in King *et al.* (2010). In our analysis for cases which reach quasi-steady state, time-averaged values of heat flux and TBL properties are used.

With no internal heating, Cartesian thermal convection for incompressible fluid ($Di = 0$) display symmetric features for the TBLs. Top and bottom TBLs contain equal amount of buoyancy, so are the downwellings and upwellings (Fig. 5a). Horizontally averaged RMS velocity for the top and bottom TBLs are identical, and the average temperature in the convective core is 0.5 (Fig. 6a). The compressibility breaks the symmetry between the TBLs. For $Di = 1$ cases, the top TBL has larger temperature difference and larger flow velocity than those for the bottom TBL, and consequently cold downwellings dominate heat transfer (Figs 5b and 6b). The adiabatic temperature gradient is also evident (Figs 6b–d). These features are expected, as have been observed by Jarvis & McKenzie (1980). An increasing compressibility causes reduced flow velocity and larger lateral homogenous temperature, that is, less vigorous convection (Figs 6a–c), which leads to less efficient heat transfer (Fig. 7 and Table 2). A larger Di also causes upwelling plumes to be much weaker than downwellings (Fig. 5d). When $Di = 2$, upwelling plumes can hardly be produced, even with a very large Ra (e.g. Fig. 5d with $Ra = 3 \times 10^9$), because at large Di, the compressibility cools the upwelling plumes rapidly to diminish the plumes (Leng & Zhong 2008a).

We computed cases with dissipation number $Di = 0$, 0.5, 1, 1.5 and 2 and a large range of Ra (Table 2). The smallest Ra for each Di is generally slightly larger than the corresponding Ra_c. In the following subsections, we will first present numerical results, and then develop a scaling theory on how Di and Ra control TBL properties and heat transfer. We will show that our theoretical analysis is consistent with the numerical results.

4.1 Numerical results of *Nu* and TBL properties

The Nusselt number is defined as the ratio of the heat flux through the convection system to the heat flux which would exist in a purely conductive state:

$$Nu = \frac{Q}{k\Delta T/d} = q, \tag{26}$$

where Q is the dimensional convective heat flux, $k\Delta T/d$ is dimensional heat flux in a purely conductive state and q is the dimensionless heat flux, given how the equations are normalized in eq. (8).

Fig. 7 shows Nu versus Ra for all the cases. For a given Di, in general, Nu does not follow a straight line in the log-log plot at small Ra. This is because at relatively small Ra, the top and bottom TBLs have not been fully developed and separated. In the following analysis on $Nu \sim Ra$ scaling, we choose cases with relatively large Ra (Table 3) that have developed vigorous convection and with Nu larger than 4. Those cases follow $Nu \sim Ra^{\alpha}$ and are along straight lines in Fig. 7.

Convective heat transfer is controlled by TBL properties. We quantified the thickness δ_l and temperature difference ΔT_l of the top and bottom TBLs from numerical models. The methods for quantifying the TBL properties are described in Appendix B. For a given Di, both the top and bottom TBL thicknesses, δ_t and δ_b, decrease with Ra (Fig. 8a). For incompressible convection ($Di = 0$), δ_l scales as $\delta_l \sim Ra^{-0.30}$ from fitting our numerical results, which agrees with

Table 2. Calculations for 2-D Cartesian compressible convection.

Case	*Di*	*Ra*	I.C.	Steps (10^4)	Grid	ΔNu (per cent)	*Nu*	ε_{Nu}	V_t	V_b
NC0013	0	10^3	0	2	65 × 65	0.002	1.47	0	4.43	4.43
NC0033	0	3×10^3	0	2	65 × 65	0.001	3.10	0	16.59	16.59
NC0053	0	5×10^3	0	2	65 × 65	0.001	3.81	0	24.90	24.90
NC0014	0	10^4	0	2	65 × 65	0.003	4.89	0	41.47	41.47
AC0034	0	3×10^4	0	2	65 × 65	0.002	7.09	0	88.61	88.62
AC0015	0	10^5	0	4	65 × 65	0.002	10.5	0	197.8	197.8
AC0035	0	3×10^5	AC0015	6	65 × 65	0.009	14.9	0	406.3	406.4
AC0016	0	10^6	0	6	65 × 65	0.003	21.7	0	882.9	882.9
AC0036	0	3×10^6	0	6	65 × 65	0.007	30.2	0	1789	1788
AC0017	0	10^7	∗	12	129 × 129	0.112	44.7	0	3867	3863
AC0037	0	3×10^7	AC0017	18	257 × 257	0.938	61.9	0.28	7326	7388
NC0513	0.5	10^3	0	5	65 × 65	0.035	1.49	0	4.58	4.37
NC0533	0.5	3×10^3	0	2	65 × 65	0.035	2.58	0	14.31	14.02
NC0553	0.5	5×10^3	0	5	65 × 65	0.043	3.07	0	21.23	20.83
NC0514	0.5	10^4	0	5	65 × 65	0.043	3.82	0	35.05	34.37
NC0534	0.5	3×10^4	0	5	65 × 65	0.015	5.33	0	74.25	72.40
NC0564	0.5	6×10^4	0	4	65 × 65	0.005	6.54	0	117.0	113.3
NC0515	0.5	10^5	0	3	65 × 65	0.032	7.55	0	161.5	155.1
AC0535	0.5	3×10^5	0	3	65 × 65	0.111	9.00	0	252.7	224.8
AC0565	0.5	6×10^5	∗	8	129 × 129	4.534	11.3	1.60	341.1	307.1
AC0516	0.5	10^6	∗	8	129 × 129	0.132	13.0	0.40	444.6	390.1
AC0536	0.5	3×10^6	∗	8	129 × 129	4.789	17.2	1.52	529.9	464.2
AC0517	0.5	10^7	∗	10	129 × 129	1.818	23.9	2.42	1077	864.6
AC0537	0.5	3×10^7	AC0517	10	129 × 129	3.249	32.6	3.07	2032	1442
NC1013	1	10^3	0	5	65 × 65	0.075	1.21	0	2.98	2.56
NC1033	1	3×10^3	0	5	65 × 65	0.072	1.82	0	10.04	9.32
NC1014	1	10^4	0	5	65 × 65	0.075	2.47	0	24.40	23.0
NC1034	1	3×10^4	0	5	65 × 65	0.101	3.19	0	50.00	46.7
NC1015	1	1×10^5	0	1	65 × 65	0.218	3.87	0	88.89	77.47
NC1035	1	3×10^5	∗	8	129 × 129	4.14	4.82	0.82	129.3	111.6
NC1065	1	6×10^5	0	2.8	65 × 65	0.510	6.37	0	157.6	135.4
AC1016	1	10^6	0	5	65 × 65	0.078	6.87	0.20	192.4	166.5
AC1036	1	3×10^6	∗	3	129 × 129	1.159	9.44	0.97	387.6	279.3
AC1017	1	10^7	∗	10	129 × 129	2.473	13.7	1.80	798.3	503.1
AC1037	1	3×10^7	AC1037	10	129 × 129	4.646	18.9	2.14	1533	848.1
NC1533	1.5	3×10^3	0	5	65 × 65	0.148	1.11	0	3.99	2.08
NC1514	1.5	10^4	0	5	65 × 65	0.064	1.31	0	10.31	6.52
NC1534	1.5	3×10^4	0	5	65 × 65	0.038	1.49	0	19.16	12.57
NC1515	1.5	10^5	0	2	65 × 65	0.443	2.00	0	30.29	24.00
NC1535	1.5	3×10^5	∗	2.5	129 × 129	0.475	2.53	0	61.08	45.84
NC1516	1.5	10^6	∗	3.5	129 × 129	0.713	3.31	0.13	126.5	81.67
AC1536	1.5	3×10^6	∗	6	257 × 257	2.94	4.40	0.41	242.7	143.6
AC1517	1.5	10^7	∗	10	257 × 257	2.12	6.27	0.71	539.0	270.9
AC1537	1.5	3×10^7	∗	8	257 × 257	2.388	8.79	1.0	1075.2	472.6
AC1518	1.5	10^8	AC1537	8	257 × 257	5.298	12.27	1.52	2108.2	799.1
NC2034	2	3×10^4	0	3	65 × 65	0.018	1.10	0	9.06	0.51
NC2015	2	10^5	0	3	65 × 65	0.325	1.23	0	18.73	0.17
NC2035	2	3×10^5	0	5	65 × 65	0.700	1.33	0	34.63	0.20
NC2016	2	10^6	∗	2	129 × 129	1.084	1.46	0	60.4	0.38
NC2036	2	3×10^6	∗	8	257 × 257	−1.27	1.71	0.13	121.1	7.93
NC2017	2	10^7	∗	6	257 × 257	−1.23	2.16	0.18	242.2	29.46
NC2037	2	3×10^7	∗	10	385 × 385	1.645	2.79	0.33	456.3	92.84
AC2018	2	10^8	∗	4	385 × 385	1.284	3.87	0.38	1020	228.1
AC2038	2	3×10^8	∗	8	385 × 385	−1.72	5.24	0.50	1965	475.8
AC2019	2	10^9	∗	7	385 × 385	5.2613	7.27	0.71	4454	971.5
AC2039	2	3×10^9	AC2019	10	385 × 385	6.7265	10.14	0.85	7209	1666

The first six columns are for case number, *Di*, *Ra*, initial condition, the number of time steps (in 10^4) and finite element grid, respectively. NC cases do not have vigorous enough convection, while AC cases have vigorous convection and are used in scaling analysis here. For the initial condition column (I.C.), '0' stands for default initial temperature condition (i.e. eq. 24), '∗' for that from its lower resolution case and 'AC' for that from lower *Ra* case. *Nu* is for surface Nusselt number. ΔNu is the difference between the top and bottom *Nu* in percentage. ε_{Nu} is the standard deviation of surface *Nu* (0 for steady state, while nonzero ε_{Nu} is for quasi-steady state). V_t and V_b are the RMS velocity for the surface and bottom, respectively.

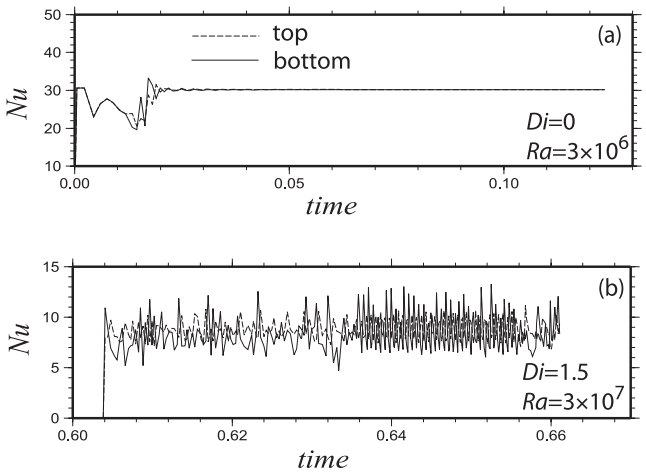

Figure 4. Nusselt number Nu versus elapsed time t for cases (a) AC0036, with $Di = 0$, $Ra = 3 \times 10^6$; (b) AC1537, with $Di = 1.5$, $Ra = 3\times10^7$. AC0036 reaches the steady state at $t = 0.04$. AC1537 reaches the quasi-steady state at about $t = 0.64$. Solid and dashed lines are Nusselt number at the bottom and top boundaries, respectively.

classic analysis, where $\delta_l \sim Ra^{-1/3}$(e.g. McKenzie *et al.* 1974). TBL thicknesses δ_l for compressible convection cases show similar scaling with Ra to that for incompressible convection (Fig. 8a). While for incompressible convection ($Di = 0$), δ_t and δ_b are identical, δ_t is larger than δ_b for compressible convection ($Di \neq 0$).

For $Di = 0$ cases, temperature difference of the top TBL,ΔT_t, is 0.5 and is identical with that of bottom TBL, ΔT_b (Fig. 9a). For $Di \neq 0$ cases, ΔT_t is larger thanΔT_b. Both ΔT_t and ΔT_b are mainly controlled by Di, and decrease dramatically with Di. For a fixed Di, both ΔT_t and ΔT_b seem to decrease slightly with Ra (Fig. 9a).

We may define a boundary layer Rayleigh number as

$$Ra_l = \frac{\rho_l^2 c_{Pl} g \alpha_l \Delta T_l \delta_l^3}{\eta_l k_l}, \tag{27}$$

where subscript l means the local value of corresponding parameters and l can be t and b, which represent the top and bottom TBLs, respectively. Note that the density for each of the TBLs, ρ_l, is taken as that at the top of the TBL.

Ra_t and Ra_b can be defined and related to Ra as

$$Ra_t = \left(\frac{\Delta T_t^*}{\Delta T^*}\right)\left(\frac{\delta_t^*}{d}\right)^3 Ra = \frac{\Delta T_t^4}{Nu^3} Ra, \tag{28}$$

$$Ra_b = e^{2Di(1-\delta_b)}\left(\frac{\Delta T_b^*}{\Delta T^*}\right)\left(\frac{\delta_b^*}{d}\right)^3 Ra = e^{2Di(1-\delta_b)}\frac{\Delta T_b^4}{Nu^3} Ra, \tag{29}$$

where the superscript $*$ denotes the dimensional values, and we considered $\rho = \rho_0 e^{Di(1-z)}$ from eq. (16) and the following relations for pure basal heating convection

$$Nu = (k\Delta T_t^*/\delta_t^*)/(k\Delta T^*/d) = (\Delta T_t^*/\Delta T^*)/(\delta_t^*/d) = \Delta T_t/\delta_t = \Delta T_b/\delta_b. \tag{30}$$

Ra_t and Ra_b calculated by (28) and (29) using numerical results of Nu, ΔT_t and ΔT_b are presented in Fig. 10. Here, we use Nu, ΔT_t and ΔT_b, but not TBL thicknesses δ_l, to determine TBL local Ra, because the latter are more difficult to quantify accurately. The most distinct feature of such determined local Ra is that for all the cases (Fig. 10)

$$Ra_t = Ra_b. \tag{31}$$

It should be noted that there are some scatterings in Fig. 10 for Ra_t and Ra_b, especially for $Di = 2$ cases that may be caused by resolution issues.

4.2 Boundary layer analysis of heat transfer

Eq. (28) can be written as

$$Nu = (\Delta T_t)^{4/3}\left(\frac{Ra}{Ra_t}\right)^{1/3}. \tag{32}$$

The scaling $Nu \sim Ra^{1/3}$ is the same as that for isoviscous and incompressible convection (e.g. McKenzie *et al.* 1974; Moresi & Solomatov 1995; Schubert *et al.* 2001). While ΔT_t is a constant (e.g. $\sim$0.5) for incompressible convection ($Di = 0$), it depends strongly on Di for compressible convection ($Di \neq 0$) (Fig. 9).

We take $Ra_t = Ra_b$ as our basic assumption in the following theoretical analysis. Combining (28) and (29), it is straightforward to obtain:

$$\frac{\Delta T_t}{\Delta T_b} = e^{Di(1-\delta_b)/2} \approx e^{Di/2}. \tag{33}$$

Since $Nu = \Delta T_t/\delta_t = \Delta T_b/\delta_b$ (i.e. eq. 30), eq. (33) leads to

$$\delta_t/\delta_b \approx e^{Di/2}. \tag{34}$$

Numerical results of $\Delta T_t/\Delta T_b$ and δ_t/δ_b for all the cases with different Ra and Di (Figs 8b and 9b) confirm eqs (33) and (34).

Our numerical results suggest that ΔT_t and ΔT_b are mainly controlled by Di. Next, we derive how ΔT_t and ΔT_b are scaled by Di. In finite amplitude compressible convection, an isentropic central region is produced (Jarvis & McKenzie 1980). In the central region, the temperature in a non-dimensional form follows (e.g. Leng & Zhong 2008a)

$$\frac{\mathrm{d}T_{ad}}{\mathrm{d}z} = -Di\,(T_{ad} + T_s), \tag{35}$$

where T_s is the non-dimensional surface temperature, T_{ad} is the adiabatic temperature and the negative sign results from z pointing upwards. Super-adiabatic temperature, which drives convection, happens in the top and bottom TBLs. We divide the convective domain vertically into three parts: the top and bottom TBLs and the central core, over which temperature differences are represented by ΔT_t, ΔT_b and ΔT_{ad}, respectively. Let ΔT be the temperature across the whole convective system, and non-dimensional$\Delta T = 1$.

$$\Delta T = 1 = \Delta T_t + \Delta T_{ad} + \Delta T_b = \Delta T_t\left(1 + \frac{\Delta T_{ad}}{\Delta T_t} + \frac{\Delta T_b}{\Delta T_t}\right). \tag{36}$$

From eq. (35), in the isentropic central area,

$$T_{ad} + T_s = Ae^{Di(1-z)}, \tag{37}$$

where A is a constant (e.g. Leng & Zhong 2008a). At the base of the top TBL or $z = 1 - \delta_t$, the temperature is $T_{ad}(z = 1 - \delta_t) = \Delta T_t$, and from eq. (37),

$$T_{ad}(z = 1 - \delta_t) + T_s = \Delta T_t + T_s = Ae^{Di\delta_t}. \tag{38}$$

Likewise, at the top of the bottom TBL or $z = \delta_b$, the temperature is $T_{ad}(z = \delta_b) = 1 - \Delta T_b$, and

$$T_{ad}(z = \delta_b) + T_s = 1 - \Delta T_b + T_s = Ae^{Di(1-\delta_b)}. \tag{39}$$

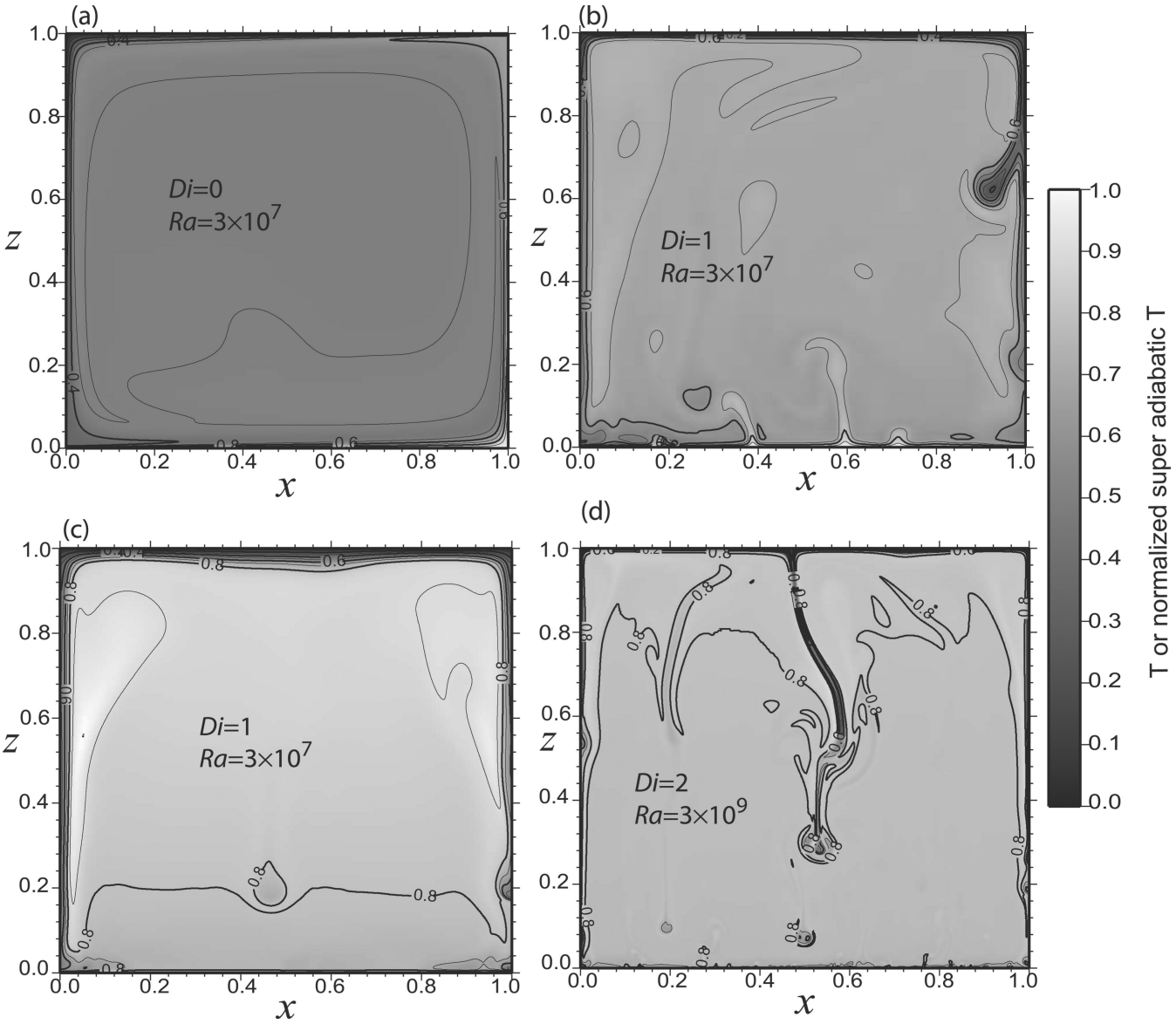

Figure 5. Contours and snapshots of representative temperature fields T for cases (a) AC0037, with $Di = 0$, $Ra = 3 \times 10^7$, and normalized super-adiabatic temperature field θ, for cases (b) AC1037, with $Di = 1$, $Ra = 3 \times 10^7$; (c) NC2037, with $Di = 2$, $Ra = 3 \times 10^7$; (d) AC2039, with $Di = 2$, $Ra = 3 \times 10^9$. The super-adiabatic temperature $T_{\rm sa}$ is computed by subtracting adiabatic temperature (for example, as shown in Fig. B1) from original temperature, and normalized super-adiabatic temperature $\theta = (T_{sa} - T_{sa}^{\min})/(T_{sa}^{\max} - T_{sa}^{\min})$, where $T_{sa}^{\max}$ and $T_{sa}^{\min}$ are the maximum and minimum of super-adiabatic temperature. $(T_{sa}^{\min}, T_{sa}^{\max})$ for cases in (b), (c) and (d) are $(-0.2803, 0.1334)$, $(-0.0713, 0.0127)$ and $(-0.0584, 0.0174)$, respectively. All the cases have reached quasi-steady states.

Combining (38) and (39) and defining $\Delta T_{ad} = T_{ad}(z = \delta_b) - T_{ad}(z = 1 - \delta_t)$, we get

$$\frac{\Delta T_{ad}}{\Delta T_t + T_s} = \frac{e^{Di(1-\delta_b)} - e^{Di\delta_t}}{e^{Di\delta_t}} = e^{Di(1-\delta_b-\delta_t)} - 1. \tag{40}$$

Substituting (40) and (33) into (36) leads to

$$1 = \Delta T_t \left[1 + \frac{\left(e^{Di(1-\delta_t-\delta_b)} - 1\right)(\Delta T_t + T_s)}{\Delta T_t} + e^{-Di/2} \right], \tag{41}$$

which can be written as

$$\Delta T_t = \frac{1 - T_s \left(e^{Di(1-\delta_t-\delta_b)} - 1\right)}{(e^{-Di/2} + e^{Di(1-\delta_t-\delta_b)})}. \tag{42}$$

From (42), ΔT_t is determined by both Di and TBL thickness $(\delta_t + \delta_b)$. As discussed before, TBL thickness δ scales with Ra following $\delta \sim Ra^{-1/3}$. Therefore, eq. (42) suggests that ΔT_t is influenced by both Di and Ra. From numerical results, $(\delta_t + \delta_b)$ is of a smaller magnitude compared with 1, especially for large Ra (Fig. 8a), and may be ignored in (42) without introducing a large error. As a result, eq. (42) may be approximated as

$$\Delta T_t \approx \frac{1 - T_s \left(e^{Di} - 1\right)}{(e^{-Di/2} + e^{Di})}. \tag{43}$$

Eq. (43) suggests that ΔT_t is mainly controlled by Di at large Ra, which agrees with numerical results (Fig. 9a). Combining eqs (33) and (43) leads to an expression for ΔT_b:

$$\Delta T_b \approx \frac{1 - T_s \left(e^{Di} - 1\right)}{(1 + e^{3Di/2})}. \tag{44}$$

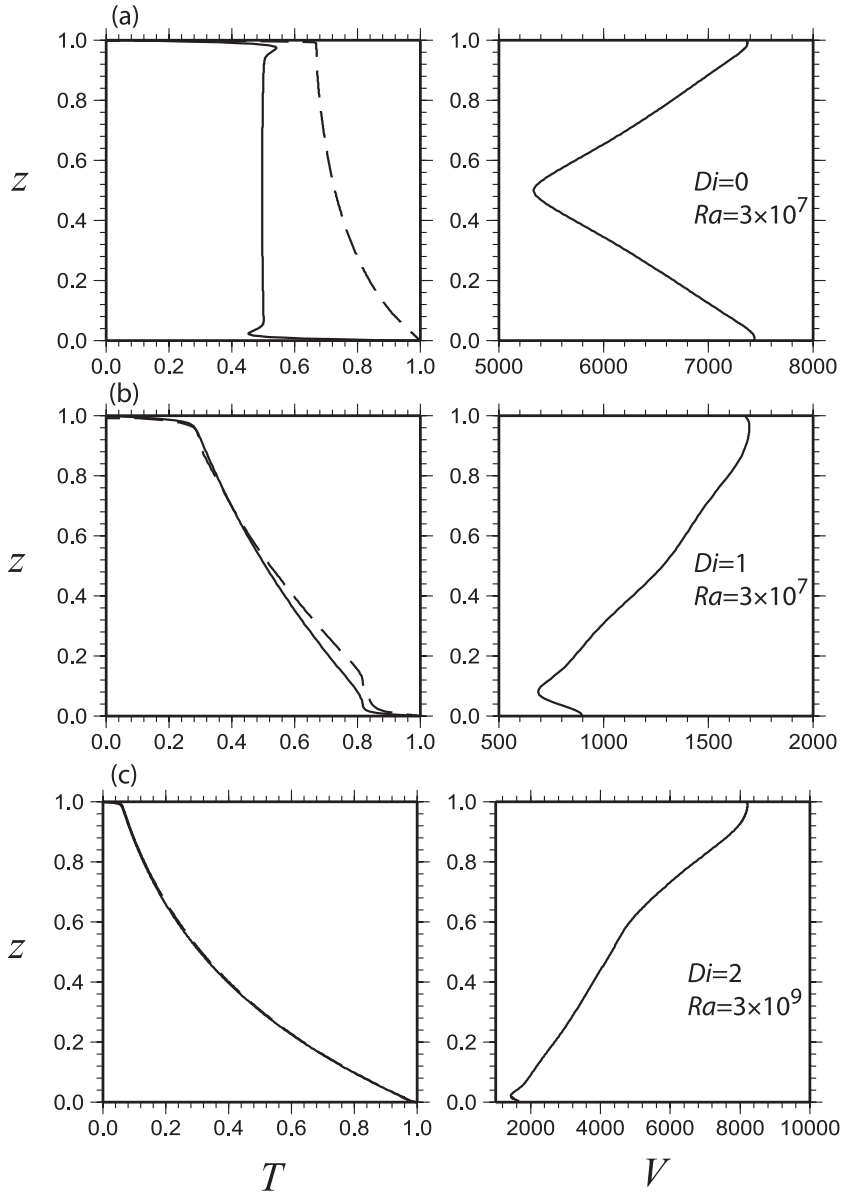

Figure 6. The solid lines are the horizontally averaged temperature (left panel) and RMS velocity (right panel) for cases (a) AC0037; (b) AC1037; (c) AC2039. The dashed lines in the temperature plots are the maximum temperature versus depth.

Fig. 11(a) shows the comparison between ΔT_t from eq. (43) and those from numerical models for different *Di* and *Ra*. For a given *Di*, both ΔT_t from the largest *Ra* case and the averaged ΔT_t for all cases (Table 3) are plotted. ΔT_t from the numerical models agree well with that predicted from the theoretical analysis (Eq. 43) with <5 per cent discrepancy, especially for cases with the largest *Ra*, and it is expected because eq. (43) is a better approximation for large *Ra* cases. ΔT_b from numerical models for different *Di* and *Ra* show similarly good agreement with those predicted from eq. (44) (Fig. 11b).

Substituting (43) into (32), we find

$$Nu = \left(\frac{1 - T_s(e^{Di} - 1)}{e^{-Di/2} + e^{Di}}\right)^{4/3} \left(\frac{Ra}{Ra_t}\right)^{1/3}. \quad (45)$$

From Fig. 10, Ra_t is approximately a constant of 18 for $Di \neq 0$ cases. Using $Ra_t = 18$ for $Di \neq 0$ cases and $Ra_t = 6$ for $Di = 0$ in eq. (45), Fig. 12 shows the comparison of *Nu* from (45) with our numerical results for all the cases with different *Ra* and *Di*. This comparison suggests that our theory as given by eq. (45) describes the numerical results of heat transfer well.

5 DISCUSSION

In this study, we formulate a 2-D Cartesian compressible convection model to examine the effects of compressibility on thermal convection. We present a new implementation of propagator matrix technique for marginal linear stability analysis and determine critical Rayleigh number for different dissipation numbers *Di* and wavenumbers k_x. In the regime of finite amplitude convection, we use a finite element code to study the influence of *Di* on TBL properties and heat flux for models with $k_x = \pi$ and different *Di* and *Ra*. We also develop scaling laws that describe the dependence of TBL properties and heat flux on *Di* and *Ra*.

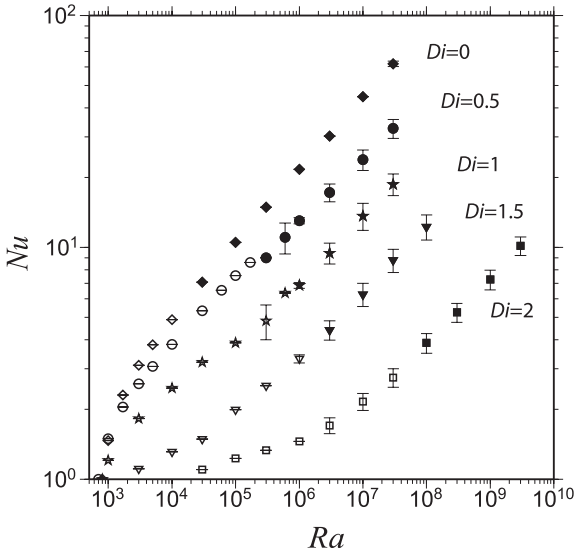

Figure 7. *Nu* versus *Ra* in log-log plot for 2-D compressible convection with different *Di*. The symbols diamond, circle, star, triangle and square are for cases with $Di = 0$, 0.5, 1, 1.5 and 2, respectively. The cases along the straight lines with filled symbols have developed vigorous convection and are used in the scaling analyses (Table 3). When applicable, error bars represent standard deviations.

5.1 Marginal linear stability analysis

Using a propagator matrix method, we have determined the critical Rayleigh number, Ra_c, for compressible convection with *Di* varying from 0 to 3. Its agreement with Ra_c determined from numerical experiments proves the robustness of the method and results. Our results indicate that if defined with surface density, Ra_c does not vary monotonically with *Di*. For example, with horizontal perturbation wavenumber $k_x = \pi$, Ra_c decreases from 779 for $Di = 0$ to 681 for $Di = 0.6$, but Ra_c increases rapidly with *Di* for $Di > 0.6$ (Fig. 1d). To show the robustness of the result, we computed two cases with $Di = 0$ and 0.5, respectively, but with the same $Ra = 730$ and $k_x = \pi$, using our finite element model. Note that $Ra = 730$ is slightly smaller than $Ra_c = 779$ for $Di = 0.0$ but larger than $Ra_c = 683$ for $Di = 0.5$. The initial temperature perturbations for these calculations are the same as described in Section 3.2. Fig. 3 shows that with same $Ra_c = 730$, the kinetic energy E_k increases with time to a steady-state value for $Di = 0.5$ case, but decays to nearly zero for $Di = 0$ case, confirming that Ra_c is smaller for $Di = 0.5$ than for $Di = 0$. However, it should be pointed out that if we re-define *Ra* using the averaged density rather than the surface density as in eq. (12), Ra_c does increase monotonically with *Di* (Fig. 1d).

Our results appear significantly different from those by Jarvis & McKenzie (1980), where the authors found that Ra_c increases much more rapidly with *Di* for models with heat flux boundary conditions at the bottom. For example, for $k_x = \pi$, Jarvis & McKenzie (1980) reported that Ra_c defined by the average density increased from 586.8 for $Di = 0$ to 9310 for $Di = 0.117$, and to 2.6×10^5 for $Di = 0.5$. It is interesting that the bottom heat flux boundary may have such a major influence on Ra_c.

Eigenfunctions for the fundamental mode and $k_x = \pi$ (Fig. 2) show that as *Di* increases, the flow in the lower region becomes more sluggish than that in the upper region. For $Di = 2$, there is an internal node in the eigenfunction of vertical velocity, indicating a shear driven flow in the lower region. This is similar to the eigenfunction results by Jarvis & McKenzie (1980). One important conclusion from our study is that the eigenfunctions of temperature $T_0(z)$, horizontal and vertical velocities $U(z)$ and $V(z)$, for compressible convection may differ significantly from sinusoidal functions

Table 3. TBL properties of finite-amplitude convection cases.

Cases	*Di*	*Ra*	ΔT_t	ΔT_b	δ_t	δ_b	Ra_t	Ra_b
AC0034	0	3×10^4	0.500	0.500	0.112	0.112	5.25	5.24
AC0015	0	10^5	0.495	0.495	0.075	0.075	5.19	5.19
AC0035	0	3×10^5	0.496	0.497	0.054	0.054	5.50	5.50
AC0016	0	10^6	0.497	0.497	0.038	0.038	5.94	5.94
AC0036	0	3×10^6	0.500	0.500	0.028	0.028	6.80	6.79
AC0017	0	10^7	0.497	0.496	0.019	0.019	6.80	6.76
AC0037	0	3×10^7	0.485	0.500	0.014	0.014	7.03	7.95
AC0535	0.5	3×10^5	0.409	0.305	0.072	0.056	11.5	9.16
AC0565	0.5	6×10^5	0.404	0.291	0.059	0.045	11.9	7.33
AC0516	0.5	10^6	0.389	0.296	0.047	0.037	10.4	9.08
AC0536	0.5	3×10^6	0.389	0.291	0.036	0.029	13.4	11.0
AC0517	0.5	10^7	0.381	0.293	0.026	0.021	15.6	14.4
AC0537	0.5	3×10^7	0.378	0.298	0.019	0.016	17.8	18.4
AC1016	1	10^6	0.269	0.168	0.061	0.038	16.1	16.9
AC1036	1	3×10^6	0.262	0.158	0.044	0.026	16.9	15.6
AC1017	1	10^7	0.255	0.156	0.030	0.019	16.7	16.4
AC1037	1	3×10^7	0.251	0.156	0.022	0.014	17.8	19.1
AC1536	1.5	3×10^6	0.154	0.073	0.053	0.023	19.6	19.1
AC1517	1.5	10^7	0.146	0.063	0.036	0.014	18.4	12.5
AC1537	1.5	3×10^7	0.140	0.063	0.025	0.011	17.2	13.5
AC1518	1.5	10^8	0.137	0.062	0.018	0.008	19.1	15.6
AC2018	2	10^8	0.059	0.023	0.023	0.007	21.2	26.6
AC2038	2	3×10^8	0.056	0.024	0.017	0.006	20.8	34.4
AC2019	2	10^9	0.054	0.022	0.012	0.004	22.1	35.3
AC2039	2	3×10^9	0.053	0.020	0.008	0.003	22.6	24.3

ΔT_t and ΔT_b are the temperature differences across the top and bottom TBLs, respectively. δ_t and δ_b are the thicknesses of the top and bottom TBLs, respectively. Ra_t and Ra_b are local Rayleigh numbers of the top and bottom TBLs, respectively.

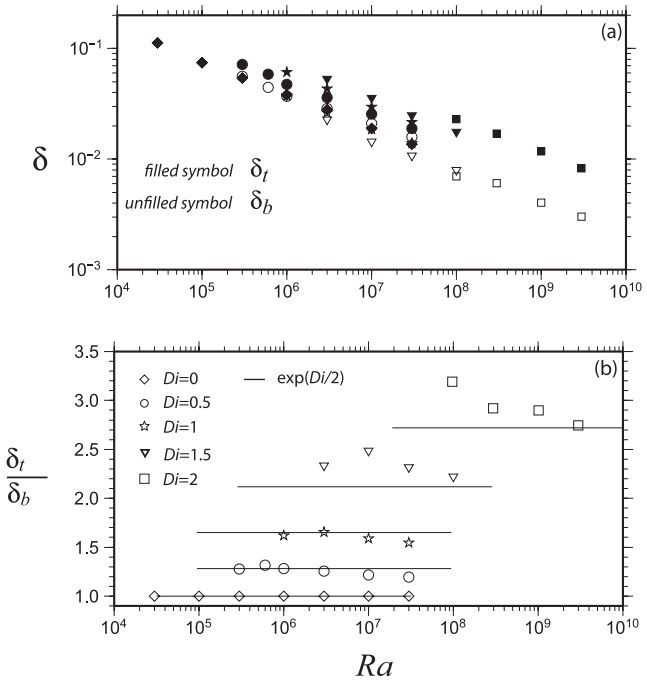

Figure 8. (a) Thicknesses of the top and bottom TBLs and (b) the ratio of top TBL thickness to bottom TBL thickness versus *Ra*. In both (a) and (b), the symbols diamond, circle, star, triangle and square represent cases with $Di = 0$, 0.5, 1, 1.5 and 2, respectively. In (a), the filled symbols are for top TBL thickness and the unfilled ones are for bottom TBL thickness. In (b), the lines mark $e^{Di/2}$.

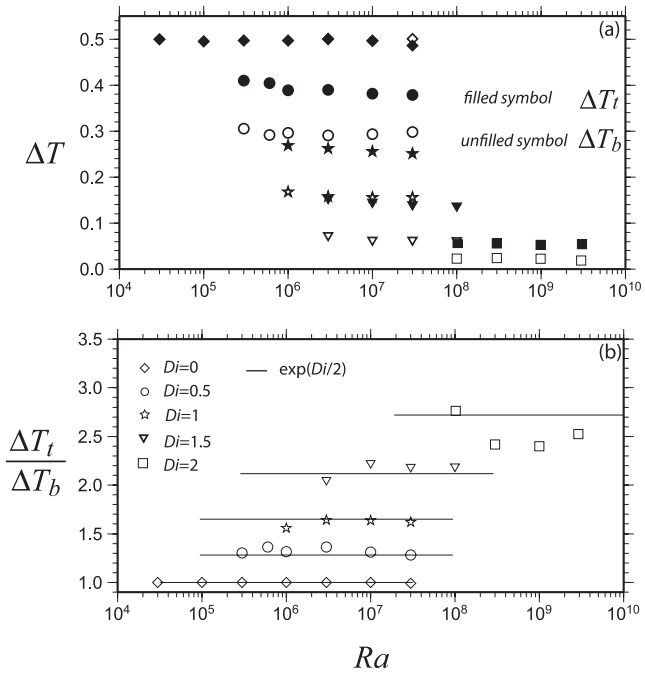

Figure 9. (a) Temperature differences across the top and bottom TBLs and (b) the ratio of temperature differences across the top TBL to that of the bottom TBL versus *Ra*. For both (a) and (b), the symbols diamond, circle, star, triangle and square are for cases with $Di = 0$, 0.5, 1, 1.5 and 2, respectively. In (a), the filled symbols are for top TBL thickness and the unfilled ones are for bottom TBL thickness. In (b), the lines mark $e^{Di/2}$.

that are eigenfunctions for a homogeneous and incompressible fluid (e.g. Turcotte & Schubert 2002). We also found that even for incompressible convection, depth-dependent thermodynamic parameters such as thermal conductivity or thermal expansion can also cause $T_0(z)$, $U(z)$ and $V(z)$ to deviate from sinusoidal functions (Figs 2c and d). For example, for incompressible convection with thermal conductivity increasing linearly from 1 at the top to 2 at the bottom, our analysis revealed that $Ra_c = 1166$ for $k_x = \pi$ and the corresponding eigenfunctions are given in Fig. 2c. Note that for this calculation, the background conductive temperature T_r needs to be determined for the variable thermal conductivity, and dT_r/dz in the propagator matrix should be modified accordingly. We also considered a case with thermal expansion decreasing linearly from 1 at the top to 0.2 at the bottom, and for this case, Ra_c is 1295 for $k_x = \pi$ and eigenfunctions are given in Fig. 2(d). These results of Ra_c are in agreement with those determined from numerical experiments, provided that the corresponding eigenfunctions $T_0(z)$ are used as initial temperature in the calculations. Compared with $Ra_c = 779$ for thermal convection in an incompressible and homogenous fluid, our results show that the depth-dependence of the thermodynamic parameters considered here stabilizes the convection.

A final remark on the marginal stability analysis is on ignoring the imaginary part of the growth rate in our analysis (i.e. we only considered real number for the growth rate), while Jarvis & McKenzie (1980) considered both imaginary and real numbers for the growth rate. The growth rate with imaginary number implies oscillatory behaviour. Although it is of some interest for future studies to examine the physical significance of imaginary part of the growth rate, we would like to point out that the independent verification of our marginal stability analysis from our finite element modelling (Figs 1b–d) suggests that our analysis is robust.

5.2 Finite amplitude compressible convection

We have quantified convective heat flux and TBL properties for compressible convection at different *Ra* and *Di*. It is well known that for isoviscous and incompressible convection, the top and bottom TBLs are symmetric with both TBL thickness and temperature difference in TBL identical for the top and bottom TBLs. Compressibility breaks the symmetry. Eqs (33) and (34) show that the ratios of thickness and temperature drop of the top TBL to those of the bottom TBL increase with *Di* but are insensitive to *Ra*, especially at large *Ra*, and these two equations describe the numerical results reasonably well (Figs 8b and 9b).

We also developed theoretical expressions for temperature differences across the top and bottom TBLs, ΔT_t and ΔT_b. We found that ΔT_t and ΔT_b, given by eqs (43) and (44), respectively, are controlled by *Di* and insensitive to *Ra*, especially when *Ra* is large and boundary layer thicknesses are significantly smaller than the depth of the fluid (see eq. 42). ΔT_t and ΔT_b from eqs (43) and (44) are consistent with numerical results (Fig. 11).

Note that eqs (43) and (44) for ΔT_t and ΔT_b may pose an upper bound on dissipation number *Di*, $Di_{\max}$, for which these equations are applicable. That temperature differences ΔT_t and ΔT_b must be greater than zero requires that

$$1 - T_s(e^{Di} - 1) > 0. \tag{46}$$

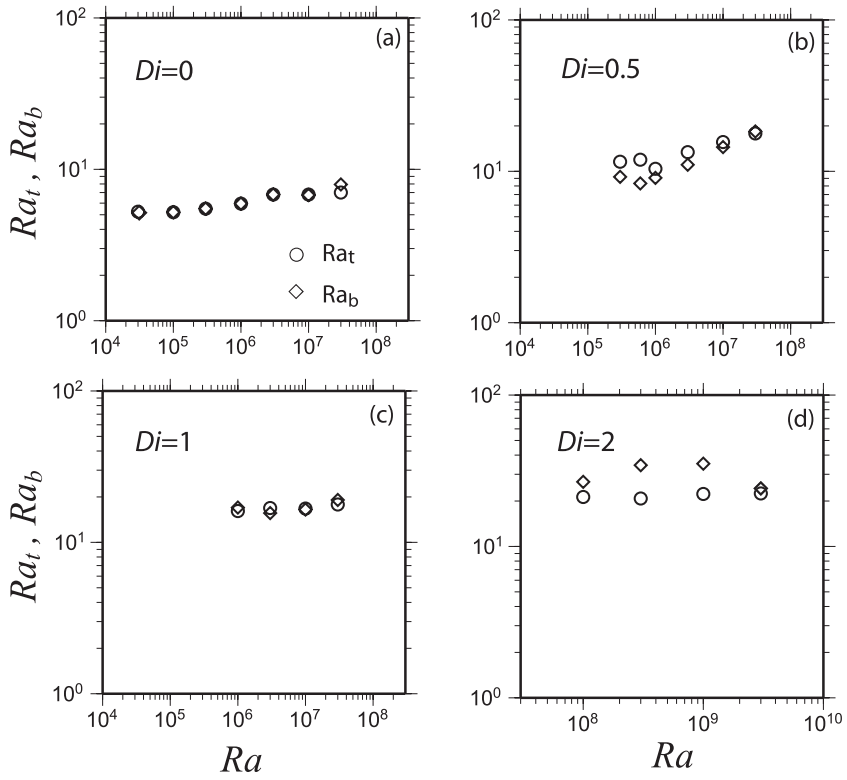

Figure 10. Boundary layer Raleigh numbers for the top and bottom TBLs versus *Ra* for cases with (a) $Di = 0$; (b) $Di = 0.5$; (c) $Di = 1$; (d) $Di = 2$. The circles and the diamonds represent the top and bottom TBLs, respectively.

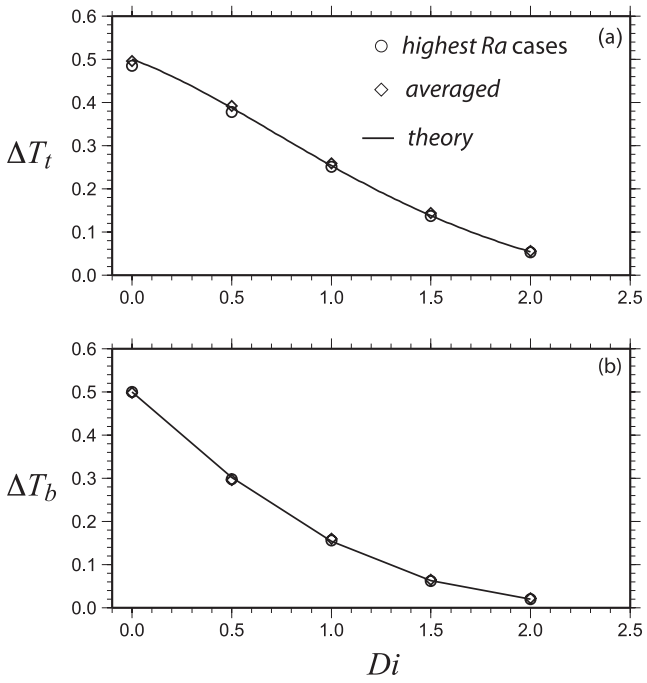

Figure 11. Temperature difference for (a) the top and (b) bottom TBLs versus *Di*. In (a) and (b), the lines are computed from eqs (43) and (44), respectively, and the circles and diamonds are from numerical experiments. The circles are from the highest *Ra* case for each *Di* series, while the diamonds are for averaged temperature difference for each *Di* series.

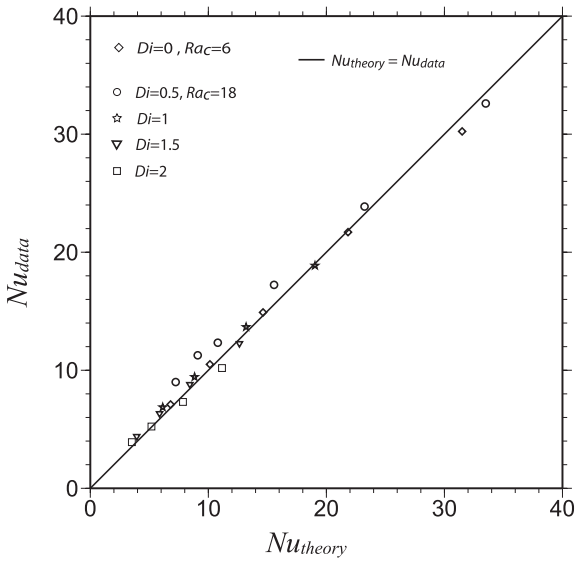

Figure 12. *Nu* from numerical results compared with those from eq. (45) for cases listed in Table 3. The line represents $Nu_{\text{data}} = Nu_{\text{theory}}$. The symbols are for *Nu* from eq. (45), using $Ra_c = 18$ for $Di > 0$ cases and $Ra_c = 6$ for $Di = 0$ cases. The symbols diamond, circle, star, triangle and square are for $Di = 0$, 0.5, 1, 1.5 and 2 cases, respectively.

In our models, the dimensional surface temperature T_s is set as 0.091 and is applicable to the Earth. To satisfy (46), *Di* must be smaller than ~2.5 or $Di_{\max} \sim 2.5$. This is consistent with the diminished bottom TBLs in cases with very high *Di* (e.g. $Di = 2$, $Ra = 3 \times 10^9$, in Fig. 6c). $Di_{\max}$ is controlled by T_s. The larger T_s is, the smaller ΔT_t and $Di_{\max}$ are. Also, note that T_s does not affect ΔT_t for $Di = 0$, because $e^{Di} - 1 = 0$.

Based on our analyses of TBL properties, we developed a scaling relationship of heat flux (i.e. *Nu*) to Rayleigh number *Ra* and dissipation number *Di* for isoviscous and basal heating compressible convection at relatively large *Ra* (Eq. 45). In particular, we found

that Nu scales with $Ra^{1/3}$, which is similar to that for incompressible thermal convection (e.g. Turcotte & Schubert 2002), while its dependence on Di follows a more complicated expression due to the relationship of ΔT_t to Di in eq. (43). Ra_t is needed to fully determine Nu in addition to Ra and Di, using eq. (45). From numerical modelling, Ra_t does not vary with Ra, but appears to increase moderately with Di from $Ra_t \sim 6$ for $Di = 0$ to $Ra_t \sim 18$ for $Di = 2$ (Fig. 10). For $Di = 0$ cases, Ra_t may be deduced from eq. (28) together with $\Delta T_t = 0.5$ and numerical results of $Nu = 0.2987Ra^{0.31}$, and this leads to $Ra_t \sim 6$, which is consistent with $Ra_t \sim 6$ in Fig. 10. Similar value of Ra_t can be obtained if $Nu = 0.294Ra^{1/3}$ from Turcotte & Schubert (2002) is used for incompressible convection. If we simply take $Ra_t = 6$ for $Di = 0$ and $Ra = 18$ for $Di > 0$, Nu predicted from eq. (45) agree well with numerical results (Fig. 12).

An interesting question is to understand the dependence of Ra_t on Di. Unfortunately, critical Rayleigh numbers Ra_c from our marginal stability analysis do not seem to be directly applicable to understand the effects of Di on $Ra_{t,}$ since Ra_c does not vary significantly for Di varying from 0 to 1 (Fig. 1b). However, Ra_c increases rapidly with decreasing convective wavelength or increasing wavenumber k_x for $k_x > \pi$ (Fig. 1b). We speculate that the dependence of Ra_t on Di (Fig. 10) may also reflect the effects of decreasing convective wavelengths for cases with increasing Di (Fig. 5). We will leave this for future studies.

Finally, we wish to point out that the $Nu \sim Ra$ scaling law (i.e. eq. 45) does not apply for convection at intermediate Ra (Fig. 7). We think that this is because at intermediate Ra, TBLs are not yet fully developed, and the top and bottom TBLs have not been separated yet.

6 CONCLUSION

Thermal convection in an isoviscous, compressible fluid is investigated using both marginal stability analysis and finite element modelling. A technique based on a propagator matrix method is developed for marginal stability analysis of thermal convection with depth-dependent thermodynamic properties, density and viscosity. Scaling laws are developed for heat transfer and TBL properties for thermal convection in an isoviscous, compressible fluid. The conclusions can be summarized as follows.

(1) Critical Rayleigh numbers, Ra_c, at the fundamental and higher modes are determined for thermal convection in a compressible fluid. At the fundamental mode, if Ra is defined by the surface density, Ra_c may not show a monotonic variation with dissipation Di. The fundamental mode may only exist for relatively small Di.

(2) For thermal convection with depth-dependent density or thermodynamics parameters, the eigenfunctions are no longer sinusoidal functions, as they are for thermal convection in a homogeneous, incompressible fluid. For $Di > 0$, the eigenfunctions for temperature $T_0(z)$, horizontal velocity $U(z)$ and vertical velocity $V(z)$ have larger amplitudes at the shallower depth than those at the larger depths, and shear driven convective cell may appear for large Di.

(3) Ra_c are also determined from numerical experiments for different Di and wavelengths. With the eigenfunctions for temperature $T_0(z)$ as initial perturbations, numerically determined Ra_c agree well with Ra_c computed from marginal stability analysis.

(4) TBL properties are quantified in numerical models of thermal convection in a compressible fluid at different Ra and Di. TBL thicknesses and temperature differences are heavily influenced by Di. While temperature differences across the TBLs decrease with Di, TBL thicknesses increase with Di. The ratios of top TBL thickness and temperature difference to corresponding bottom TBL properties are $e^{Di/2}$. For both incompressible and compressible convection, TBL thicknesses follow $\delta_l \sim Ra^{-1/3}$, while TBL temperature differences are insensitive to Ra.

(5) Our numerical modelling shows that the local Rayleigh numbers at the top and bottom TBLs are nearly identical and are insensitive to Ra and Di for compressible convection.

(6) The scaling laws of the temperature differences across TBLs, ΔT_t and ΔT_b, are derived as $\Delta T_t = [1 - T_s(e^{Di} - 1)]/(e^{-Di/2} + e^{Di})$ and $\Delta T_b = [1 - T_s(e^{Di} - 1)]/(1 + e^{3Di/2})$. ΔT_t and ΔT_b are found only dependent on Di. The scaling laws are verified by numerical results.

(7) The scaling law of heat transfer, Nusselt number Nu, for thermal convection in an isoviscous, compressible fluid is derived to be $Nu = \left(\frac{1-T_s(e^{Di}-1)}{e^{-Di/2}+e^{Di}}\right)^{4/3}\left(\frac{Ra}{Ra_t}\right)^{1/3}$. Nu scales with Ra as $Nu \sim Ra^{1/3}$, similar with that for incompressible convection. The scaling law for Nu is consistent with numerical modelling results. We think that these results may have important implications for understanding thermal evolution of super-Earths.

ACKNOWLEDGEMENTS

This work was supported by NSF grant EAR-1015669. We wish to thank Drs. Jonathan Besserer, Masanori Kameyama, an anonymous reviewer and Associate Editor Stephane Labrosse for their careful and constructive reviews.

REFERENCES

Balachandar, S., Yuen, D.A. & Reuteler, D., 1992. Time-dependent three-dimensional compressible convection with depth-dependent properties, *Geophys. Res. Lett.,* **19**(22), 2247–2250.

Bercovici, D., Schubert, G. & Glatzmaier, G., 1992. Three-dimensional convection of an infinite-Prandtl-number compressible fluid in a basally heated spherical-shell, *J. Fluid Mech.,* **239,** 683–719.

Birch, F., 1952. Elasticity and constitution of the earth interior, *J. geophys. Res.,* **57**(2), 227–286.

Buffet, B.A., Gable, C.W. & O'Connell, R.J., 1994. Linear stability of a layered fluid with mobile surface plates, *J. geophys. Res.,* **99**(B10), 19 885–19 900.

Charbonneau, D. *et al.* 2009. A super-Earth transiting a nearby low-mass star, *Nature,* **462**(7275), 891–894.

Foley, B.J., Bercovici, D. & Landuyt, W., 2012. The conditions for plate tectonics on super-Earths: inferences from convection models with damage, *Earth planet. Sci. Lett.,* **331–332**(2012), 281–290.

Gilbert, F. & Backus, G.E., 1966. Propagator matrices in elastic wave and vibration problems, *Geophysics,* **31**(2), 326–332.

Hager, B.H. & O'Connell, R.J., 1981. A simple global-model of plate dynamics and mantle convection, *J. geophys. Res.,* **86**(B6), 4843–4867.

Ita, J. & King, S.D., 1994. Sensitivity of convection with an endothermic phase-change to the form of governing equations, initial conditions, boundary conditions, and equation of state, *J. geophys. Res. Solid Earth,* **99**(B8), 15 919–15 938.

Jarvis, G.T. & McKenzie, D.P., 1980. Convection in a compressible fluid with infinite Prandtl number, *J. Fluid Mech.,* **96**(03), 515–583.

Jeffreys, H., 1930. The instability of a compressible fluid heated below, *Math. Proc. Camb. Phil. Soc.,* **26,** 170–172.

King, S.D., Lee, C., van Keken, P.E., Leng, W., Zhong, S.J., Tan, E., Tosi, N. & Kameyama, M.C., 2010. A community benchmark for 2-D Cartesian compressible convection in the Earth's mantle, *Geophys. J. Int.,* **180**(1), 73–87.

Leng, W. & Zhong, S.J., 2008a. Viscous heating, adiabatic heating and energetic consistency in compressible mantle convection, *Geophys. J. Int.,* **173**(2), 693–702.

Leng, W. & Zhong, S.J., 2008b. Controls on plume heat flux and plume excess temperature, *J. geophys. Res. Solid Earth,* **113,** B04408, doi:10.1029/2007JB005155.

McKenzie, D.P, Roberts, J.M. & Weiss, N.O., 1974. Convection in Earth's mantle: towards a numerical-simulation, *J. Fluid Mech.,* **62**(3), 465–538.

Moresi, L.N. & Solomatov, V.S., 1995. Numerical investigation of 2d convection with extremely large viscosity variations, *Phys. Fluids,* **7**(9), 2154–2162.

Moresi, L., Zhong, S.J. & Gurnis, M., 1996. The accuracy of finite element solutions of Stokes' flow with strongly varying viscosity, *Phys. Earth planet. Inter.,* **97**(1–4), 83–94.

O'Neill, C. & Lenardic, A., 2007. Geological consequences of super-sized Earths, *Geophys. Res. Lett.,* **34,** L19204, doi:10.1029/2007GL030598.

Schubert, G., Turcotte, D.L. & Olson, P., 2001. *Mantle Convection in the Earth and Planets,* Cambridge University Press, New York, 940p.

Steinbach, V., Hansen, U. & Ebel, A., 1989. Compressible convection in the Earth's mantle—a comparison of different approaches, *Geophys. Res. Lett.,* **16**(7), 633–636.

Tackley, P.J., 1996. Effects of strongly variable viscosity on three-dimensional compressible convection in planetary mantles, *J. geophys. Res.,* **101**(B2), 3311–3332.

Tan, E. & Gurnis, M., 2005. Metastable superplumes and mantle compressibility, *Geophys. Res. Lett.,* **32,** L20307, doi:10.1029/2005GL024190.

Tan, E., Leng, W., Zhong, S.J. & Gurnis, M., 2011. On the location of plumes and lateral movement of thermochemical structures with high bulk modulus in the 3-D compressible mantle, *Geochem. Geophys. Geosyst.,* **12,** Q07005, doi:10.1029/2011GC003665.

Turcotte, D.L. & Schubert, G., 2002. *Geodynamics,* Cambridge University Press, New York, pp. 267–272

Thompson, P.F. & Tackley, P.J., 1998. Generation of mega-plumes from the core-mantle boundary in a compressible mantle with temperature-dependent viscosity, *Geophys. Res. Lett.,* **25**(11), 1999–2002.

Valencia, D., Sasselov, D.D. & O'Connell, R.J., 2007. Radius and structure models of the first super-Earth planet, *Astrophys. J.,* **656**(1), 545–551.

Van Heck, H.J. & Tackley, P.J., 2011. Plate tectonics on super-Earths: equally or more likely than on Earth, *Earth planet. Sci. Lett.,* **310**(2011), 252–261.

Zhong, S. & Gurnis, M., 1993. Dynamic feedback between a continent-like raft and thermal-convection, *J. geophys. Res. Solid Earth,* **98**(B7), 12 219–12 232.

APPENDIX A: MARGINAL STABILITY ANALYSIS USING A PROPAGATOR MATRIX METHOD

The marginal linear stability problem for compressible flow is governed by eqs (18)–(20). Leng & Zhong (2008a) constructed a propagator matrix for the Stokes' flow problem for a compressible fluid (i.e. eqs 18 and 19). Based on their method, we add the linearized energy equation (20) and set up the propagator matrix for the marginal linear stability problem. In the linearized governing eqs (18)–(20), the dependences of the velocities, pressure and stresses perturbations on x and z are separable. Horizontal component of the perturbations is represented by sinusoidal functions, but vertical component of the perturbations is represented by arbitrary functions. The time-dependence of the perturbations is expressed by an exponential function of time with a growth rate α'. The perturbations should satisfy boundary conditions. The free-slip boundary condition requires that $\tau'_{xz} = u' = 0$ at $x = 0$ and 1, and $\tau'_{xz} = v' = 0$ at $z = 0$ and 1. The fixed temperature boundary condition requires that $T' = 0$ at $z = 0$ and 1. The perturbations can be expressed in Fourier transform as

$$
\begin{aligned}
T' &= \int T_0(z)\cos(\mathrm{k}_x x)\, e^{\alpha' t}\mathrm{dk}_x \\
u' &= \int U(z)\sin(\mathrm{k}_x x)\, e^{\alpha' t}\mathrm{dk}_x \\
v' &= \int V(z)\cos(\mathrm{k}_x x)\, e^{\alpha' t}\mathrm{dk}_x, \\
\tau'_{xz} &= \int Y_{xz}(z)\sin(\mathrm{k}_x x)\, e^{\alpha' t}\mathrm{dk}_x \\
\sigma'_{zz} &= \int S_{zz}(z)\cos(\mathrm{k}_x x)\, e^{\alpha' t}\mathrm{dk}_x
\end{aligned}
\tag{A1}
$$

where k_x is the horizontal wavenumber, $T_0(z)$, $U(z)$, $V(z)$, $Y_{xz}(z)$ and $S_{zz}(z)$ represent the vertical dependence of the perturbations corresponding to k_x. The boundary conditions $T' = v' = \tau' = 0$ at $z = 0$ and 1 require that

$$
T_0 = V = Y_{xz} = 0 \ \text{ at } z = 0 \text{ and } 1. \tag{A2}
$$

Linearized governing eqs (18)–(20) should be formulated into a vector linear differential eq. (22) so that it can be solved by a propagator matrix method. Based on a velocity–stress formulation, the vector W in eq. (22) is chosen as (23). Linearized governing equations and constitutive equation are rearranged such that only items in vector W are used in the equations as unknown variables. In the following equations, non-dimensional forms are used and the variables with a prime are perturbations in the linearized equations.

Considering the depth-dependent density profile (16), non-dimensional linearized mass conservation equation (18) can be rewritten as

$$
\left(\rho_r u'_i\right)_{,i} = \rho_{r,i} u'_i + \rho_r u'_{i,i} = -Di\, e^{Di(1-z)} v' + e^{Di(1-z)} u'_{i,i} = 0, \tag{A3}
$$

or

$$
\frac{\partial u'}{\partial x} + \frac{\partial v'}{\partial z} - v' Di = 0, \tag{A4}
$$

The total stress σ_{ij} can be related to dynamic pressure p and deviatoric stress τ_{ij} as

$$\sigma_{ij} = -p\delta_{ij} + \tau_{ij}, \tag{A5}$$

where τ_{ij} is given in eq. (7). From eq. (A5), σ_{zz} and p are

$$\sigma_{zz} = -p + \eta\left[2\frac{\partial v}{\partial z} - \frac{2}{3}\left(\frac{\partial u}{\partial x} + \frac{\partial v}{\partial z}\right)\right], \tag{A6}$$

$$p = \frac{4}{3}\eta\frac{\partial v}{\partial z} - \frac{2}{3}\eta\frac{\partial u}{\partial x} - \sigma_{zz}. \tag{A7}$$

Substituting (A7) into the x component momentum conservation eq. (19) leads to

$$\frac{\partial \sigma'_{zz}}{\partial x} + \frac{\partial \tau'_{xz}}{\partial z} + 4\eta\frac{\partial^2 u'}{\partial x^2} - 2\eta\gamma\frac{\partial v'}{\partial x} = 0. \tag{A8}$$

Substituting (A7) into the z component of eq. (19) leads to

$$\frac{\partial \sigma'_{zz}}{\partial z} + \frac{\partial \tau'_{xz}}{\partial x} + Ra(\alpha g)\rho_r(T - T_r) - \frac{g}{c_P\Gamma}\alpha\gamma\left(\frac{4}{3}\eta\frac{\partial v'}{\partial z} - \frac{2}{3}\eta\frac{\partial u'}{\partial x} - \sigma'_{zz}\right) = 0. \tag{A9}$$

The non-dimensional linearized energy equation (20) may be written as

$$\rho_r c_P\dot{T}' + \rho_r c_P v'\frac{\mathrm{d}T_r}{\mathrm{d}z} + \rho_r v' Di\alpha g\Gamma(T_r + T_s) = k\left(\frac{\partial^2 T'}{\partial x^2} + \frac{\partial^2 T'}{\partial z^2}\right). \tag{A10}$$

From the constitutive equation (7),

$$\tau_{xz} = \eta\left(\frac{\partial u}{\partial z} + \frac{\partial v}{\partial x}\right). \tag{A11}$$

For each wavenumber k_x, combining eqs (A4) and (A8)–(A11), and eliminating $\sin(\mathrm{k}_x x)$, $\cos(\mathrm{k}_x x)$ and $e^{\alpha' t}$, these equations can be written as

$$\frac{\mathrm{d}U}{\mathrm{d}z} = \mathrm{k}_x V + \frac{1}{\eta}Y_{xz}, \tag{A12}$$

$$\frac{\mathrm{d}V}{\mathrm{d}z} = -\mathrm{k}_x U + \gamma V, \tag{A13}$$

$$\frac{\mathrm{d}S_{zz}}{\mathrm{d}z} = -2\eta\mathrm{k}_x\gamma\left(\frac{\alpha g}{c_P\Gamma}\right)U + \frac{4}{3}\eta\gamma^2\left(\frac{\alpha g}{c_P\Gamma}\right)V - \left(\frac{\alpha g}{c_P\Gamma}\right)\gamma - \mathrm{k}_x Y_{xz} - Ra\rho_r(\alpha g)T_0, \tag{A14}$$

$$\frac{\mathrm{d}Y_{xz}}{\mathrm{d}z} = 4\eta\mathrm{k}_x^2 U - 2\eta\mathrm{k}_x\gamma V + \mathrm{k}_x S_{zz}, \tag{A15}$$

$$\frac{\mathrm{d}}{\mathrm{d}z}T_0 = \frac{\mathrm{d}T_0}{\mathrm{d}z}, \tag{A16}$$

$$\frac{\mathrm{d}}{\mathrm{d}z}\frac{\mathrm{d}T_0}{\mathrm{d}z} = \frac{\rho_r}{k}\left[Di(\alpha g)(1 - z + T_s) - c_P\right]V + \left[\frac{\rho_r c_P\alpha'}{k} + \mathrm{k}_x^2\right]T_0. \tag{A17}$$

Eqs (A12)–(A17) may be written as a vector equation (22) or $\mathrm{d}W/\mathrm{d}z = AW$, and the vector W and the matrix A are defined in eqs (A18) and (A19):

$$\mathrm{W} = \left(V, U, \frac{S_{zz}}{2\mathrm{k}_x}, \frac{Y_{xz}}{2\mathrm{k}_x}, T_0, \frac{\mathrm{d}T_0}{\mathrm{d}z}\right)^{\mathrm{T}}, \tag{A18}$$

$$\mathrm{A} = \begin{pmatrix} Di & -\mathrm{k}_x & 0 & 0 & 0 & 0 \\ \mathrm{k}_x & 0 & 0 & \frac{2\mathrm{k}_x}{\eta} & 0 & 0 \\ \frac{2\eta g}{3c_P\Gamma}\frac{\alpha Di^2}{\mathrm{k}_x} & -\frac{g\eta}{c_P\Gamma}\alpha Di & -\frac{g}{c_P\Gamma}\alpha Di & -\mathrm{k}_x & -g\frac{\alpha Ra\rho_r}{2\mathrm{k}_x} & 0 \\ -Di\eta & 2\mathrm{k}_x\eta & \mathrm{k}_x & 0 & 0 & 0 \\ 0 & 0 & 0 & 0 & 0 & 1 \\ \frac{\rho_r\alpha g}{k}\left[Di\,(1 - z + T_s) - c_P\right] & 0 & 0 & 0 & \left(\frac{c_P\alpha'\rho_r}{k} + \mathrm{k}_x^2\right) & 0 \end{pmatrix}, \tag{A19}$$

where the superscript T for eq. (A18) represents matrix transpose. We assume that all the parameters in matrix A except for ρ_r in (A19) are constant and independent of z. This leads to dimensionless parameters g, c_P, Γ, η, α and k in eq. (A19) to be 1, and matrix A may be written as

$$\mathrm{A} = \begin{pmatrix} Di & -\mathrm{k}_x & 0 & 0 & 0 & 0 \\ \mathrm{k}_x & 0 & 0 & 2\mathrm{k}_x & 0 & 0 \\ \frac{2}{3}\frac{Di^2}{\mathrm{k}_x} & -Di & -Di & -\mathrm{k}_x & -\frac{Ra\rho_r}{2\mathrm{k}_x} & 0 \\ -Di & 2\mathrm{k}_x & \mathrm{k}_x & 0 & 0 & 0 \\ 0 & 0 & 0 & 0 & 0 & 1 \\ \rho_r\left[Di\,(1-z+T_s)-1\right] & 0 & 0 & 0 & \left(\alpha'\rho_r+\mathrm{k}_x^2\right) & 0 \end{pmatrix}. \tag{A20}$$

We then discuss solution procedures of eq. (22) using a propagator matrix method. Propagator matrix method was proposed by Gilbert & Backus (1966) and is widely used to solve vector linear differential equation in the form of eq. (22). Eq. (22) has a solution:

$$\mathrm{W}(z) = e^{\mathrm{A}(z-z_0)}\mathrm{W}(z_0) = \mathrm{P}(z, z_0)\mathrm{W}(z_0), \tag{A21}$$

where

$$\mathrm{P}(z, z_0) = e^{\mathrm{A}(z-z_0)} \tag{A22}$$

is a propagator matrix that has the same dimensions as matrix A (i.e. 6×6), and $\mathrm{W}(z_0)$ is vector W at $z = z_0$ (e.g. at a boundary). If matrix A is dependent on z, the solution at any depth can be obtained by propagating along z direction from a starting point z_0 with

$$\mathrm{W}(z_n) = \mathrm{P}(z_n, z_{n-1})\,\mathrm{P}(z_{n-1}, z_{n-2})\cdots\mathrm{P}(z_2, z_1)\,\mathrm{P}(z_1, z_0)\,\mathrm{W}(z_0) = \mathrm{P}_n\mathrm{P}_{n-1}\cdots\mathrm{P}_2\mathrm{P}_1\mathrm{W}(z_0) = \mathrm{PW}(z_0), \tag{A23}$$

where $\mathrm{P}_i = e^{\mathrm{A}_i(z_i - z_{i-1})}$ is a propagator matrix between z_i and z_{i-1} over which $\mathrm{A_i}$ and $\mathrm{P_i}$ can be treated as constant matrices.

Given boundary conditions (A2), vectors W at $z = 1$ and $z = 0$, denoted as W_1 and W_0, respectively, are

$$\mathrm{W}_1 = \left(0, U(z=1), \frac{S_{zz}(z=1)}{2\mathrm{k}_x}, 0, 0, \frac{\mathrm{d}T_0}{\mathrm{d}z}_{z=1}\right)^{\mathrm{T}}, \tag{A24}$$

$$\mathrm{W}_0 = \left(0, U(z=0), \frac{S_{zz}(z=0)}{2\mathrm{k}_x}, 0, 0, \frac{\mathrm{d}T_0}{\mathrm{d}z}_{z=0}\right)^{\mathrm{T}}, \tag{A25}$$

and from eq. (A21)

$$\mathrm{W}_1 = \mathrm{P}(1, 0)\,\mathrm{W}_0. \tag{A26}$$

Propagator matrix P(1,0) in eq. (A26) is constructed as given in (A22) and (A23), based on a grid between $z = 0$ and $z = 1$ from z-dependent matrix A. There are six unknowns in W_1 and W_0: horizontal velocity U, vertical normal stress $S_{zz}/2\mathrm{k}_x$, and $\mathrm{d}T_0/\mathrm{d}z$ at the surface and bottom boundaries, and they are represented as x, y, z, a, b and c, respectively. Eq. (A26) can be written as

$$\begin{aligned} 0 &= \mathrm{P}_{12}a + \mathrm{P}_{13}b + \mathrm{P}_{16}c \\ 0 &= \mathrm{P}_{42}a + \mathrm{P}_{43}b + \mathrm{P}_{46}c \\ 0 &= \mathrm{P}_{52}a + \mathrm{P}_{53}b + \mathrm{P}_{56}c \\ x &= \mathrm{P}_{22}a + \mathrm{P}_{23}b + \mathrm{P}_{26}c \\ y &= \mathrm{P}_{32}a + \mathrm{P}_{33}b + \mathrm{P}_{36}c \\ z &= \mathrm{P}_{62}a + \mathrm{P}_{63}b + \mathrm{P}_{66}c \end{aligned}, \tag{A27}$$

where $\mathrm{P_{ij}}$ is the ij item of propagator matrix P(1,0). Eq. (A27) may be rearranged as

$$\begin{pmatrix} \mathrm{P}_{12} & \mathrm{P}_{13} & \mathrm{P}_{16} & 0 & 0 & 0 \\ \mathrm{P}_{42} & \mathrm{P}_{43} & \mathrm{P}_{46} & 0 & 0 & 0 \\ \mathrm{P}_{52} & \mathrm{P}_{53} & \mathrm{P}_{56} & 0 & 0 & 0 \\ \mathrm{P}_{22} & \mathrm{P}_{23} & \mathrm{P}_{26} & -1 & 0 & 0 \\ \mathrm{P}_{32} & \mathrm{P}_{33} & \mathrm{P}_{36} & 0 & -1 & 0 \\ \mathrm{P}_{62} & \mathrm{P}_{63} & \mathrm{P}_{66} & 0 & 0 & -1 \end{pmatrix} \begin{pmatrix} a \\ b \\ c \\ x \\ y \\ z \end{pmatrix} = 0. \tag{A28}$$

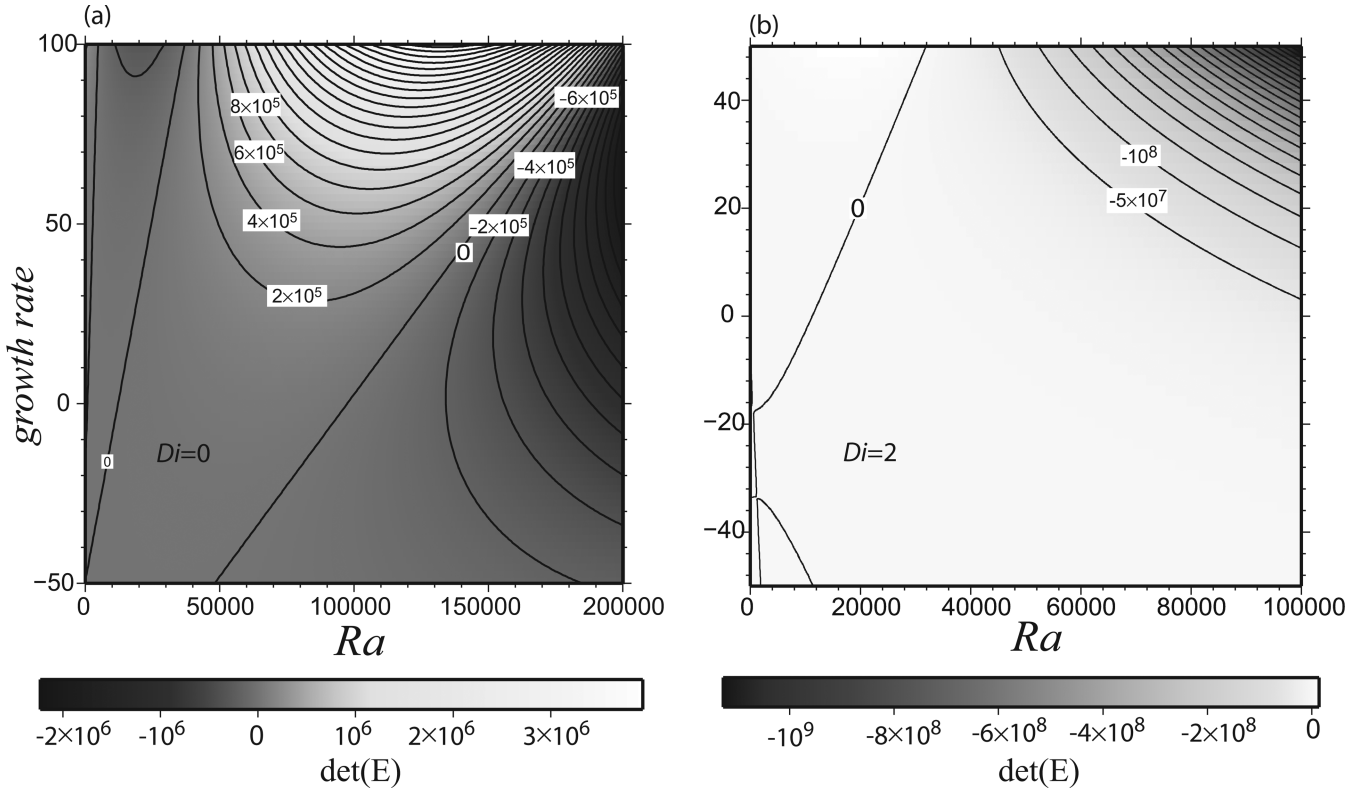

Figure A1. Contour plots of the determinant of matrix E in growth rate α' and *Ra* space for cases with $k_x = \pi$ and (a) $Di = 0$ and (b) $Di = 2$.

A non-trivial solution for eq. (A28) requires that the determinant of the 6×6 matrix in eq. (A28) is zero, which, in turn, requires

$$\det \begin{pmatrix} P_{12} & P_{13} & P_{16} \\ P_{42} & P_{43} & P_{46} \\ P_{52} & P_{53} & P_{56} \end{pmatrix} = 0. \tag{A29}$$

Eq. (A29) forms the basis of our marginal stability analysis using the propagator matrix technique.

For a given set of thermodynamic parameters, mantle compressibility, density structure and wavenumber of the perturbation, there are two unknown parameters in matrix A in (A20) or matrix E in (A29): the growth rate α' and the Rayleigh number *Ra*. Note that critical Rayleigh number Ra_c is defined as *Ra* which makes $\alpha' = 0$. A search scheme is developed to determine Ra_c: setting $\alpha' = 0$, we compute det(E) for different *Ra*, and when det(E) = 0, *Ra* equals Ra_c. Different Ra_c can be determined for different wavenumber k_x and other model parameters such as the dissipation number *Di*.

To illustrate the search scheme, we present contour plots of det(E) in the $Ra - \alpha'$ space in Fig. A1 for two calculations with $k_x = \pi$ and $Di = 0$ and $Di = 2$, respectively. For $Di = 0$, it is observed that the zero contours of det(E), which we use to find Ra_c at $\alpha' = 0$, are straight lines, indicating that in the limit of weak convection, growth rate increases linearly with *Ra*. As there are multiple zero contour lines of det(E) (Fig. A1a), more than one Ra_c can be obtained, and each Ra_c is for a distinct mode. We use $n = 0$ to represent the fundamental mode and $n = 1, 2, \ldots$ to represent the first, second, ... mode. The value of *n* represents the number of nodes where the vertical flow velocity is zero (excluding $z = 0$ and $z = 1$), and $n+1$ is the number of convection cells that are stacked in the vertical direction. For the range of *Ra* shown in Fig. A1, zero contours of det(E) cross the $\alpha' = 0$ line twice for $Di = 0$ but only once for $Di = 2$. What mode each zero contour of det(E) corresponds to depends on eigenfunction of vertical flow velocity $V(z)$.

The eigenfunctions of $T_0(z)$, $U(z)$ and $V(z)$ are also determined from the propagator matrix method. First, we need to determine $W_0 = W(z = 0)$ in eq. (A24). From eqs (A24)–(A26), we get

$$EW_0^{sub} = \begin{pmatrix} P_{12} & P_{13} & P_{16} \\ P_{42} & P_{43} & P_{46} \\ P_{52} & P_{53} & P_{56} \end{pmatrix} \begin{pmatrix} U(z=0) \\ \dfrac{S_{zz}}{2k_x}(z=0) \\ \dfrac{dT_0}{dz}_{z=0} \end{pmatrix} = 0, \tag{A30}$$

where W_0^{sub} consists of the three non-zero items of W_0. Since det(E) = 0, W_0^{sub} cannot be uniquely determined. However, we seek for a solution by fixing $dT_0/dz_{z=0} = 1$. For a given set of model parameters (e.g. *Di* and k_x), propagator matrix P(*z*,0) is formed by eqs (A22) and (A23), using $Ra_c = Ra$ and growth rate $\alpha' = 0$ in matrix A (i.e. eq. A20). With W_0 and the propagator matrix P(*z*,0), W(*z*) (i.e. the eigenfunctions) can be computed from eq. (A23). In Fig. 2, we show eigenfunctions of $T_0(z)$, $U(z)$, and $V(z)$ for some selective cases. Note

that $T_0(z)$ is scaled such as its maximum value is 1, and $U(z)$ and $V(z)$ are scaled accordingly. Based on $V(z)$, we also determined that the two modes in Fig. A1a for $Di = 0$ are for $n = 0$ and $n = 1$ modes, while the only mode in Fig. A1b for $Di = 2$ is for $n = 1$ mode. The latter suggests that for $Di = 2$, $n = 0$ mode (i.e. the fundamental mode) does not exist. In this study, we use 129 uniform grid points in z direction to compute propagator matrix for all the results shown in Section 3.2.

APPENDIX B: QUANTIFYING TBL PROPERTIES

In compressible convection, an isentropic central region is developed (e.g. Jarvis & McKenzie 1980), and the adiabatic temperature follows eq. (35). While the horizontally average temperature follows adiabatic temperature $T_{\rm ad}$ in the isentropic central regime, it deviates significantly from $T_{\rm ad}$ within the top and bottom TBLs (i.e. super-adiabatic). Here, we describe how the thicknesses and temperature difference of TBLs are defined and quantified.

As an example, Fig. B1b shows the gradients of typical horizontally averaged temperature $\mathrm{d}T/\mathrm{d}z$ and of adiabatic temperature $\mathrm{d}T_{ad}/\mathrm{d}z$ (computed from eq. 35) for case AC1017, where $Di = 1$ and $Ra = 10^7$. The temperature gradient deviates from adiabatic gradient in the top and bottom TBLs and we define the bottom (top) of the top (bottom) TBL as where the deviation of temperature gradient starts to develop:

$$\left(\left|\frac{\mathrm{d}T}{\mathrm{d}z}\right| - \left|\frac{\mathrm{d}T_{ad}}{\mathrm{d}z}\right|\right) \Big/ \left(Nu - \left|\frac{\mathrm{d}T_{ad}}{\mathrm{d}z}\right|\right) > \varepsilon. \tag{B1}$$

In (B1), ε is a small value, and in our study is set as 0.2, and $\mathrm{d}T_{\rm ad}/\mathrm{d}z$ in both numerator and denominator is the adiabatic temperature gradient at depth z. Eq. (B1) measures super-adiabatic gradient normalized by surface super-adiabatic gradient and helps to determine the top and bottom TBL thicknesses $\delta_{\rm t}$ and $\delta_{\rm b}$. The choice of ε affects the values of $\delta_{\rm t}$ and $\delta_{\rm b}$. The larger ε is, the smaller $\delta_{\rm t}$ and $\delta_{\rm b}$ are. However, we found that the ratios of TBL thicknesses and the scalings of such determined TBL properties are insensitive to the choice of ε. After $\delta_{\rm t}$ and $\delta_{\rm b}$ are determined, the temperature difference in TBLs, ΔT_t and ΔT_b can be determined from the horizontally averaged temperature profile (Fig. B1a). Interpolation is needed to obtain ΔT_t, because $\delta_{\rm t}$ and $\delta_{\rm b}$ do not necessarily occur at the grid points. For each case, we determine average TBL thickness and temperature difference over a large number of time steps for steady-state or quasi-steady state solutions. The adiabatic temperature is also plotted in Fig. B1(a). Since eq. (35) might not be applicable within TBLs, here, we assume that the adiabatic temperatures within the top and bottom TBLs are assumed to be the same as those outside the TBLs. This assumption is valid because the TBLs are very thin, and $\Delta T_{\rm ad}$ within TBLs should be very small.

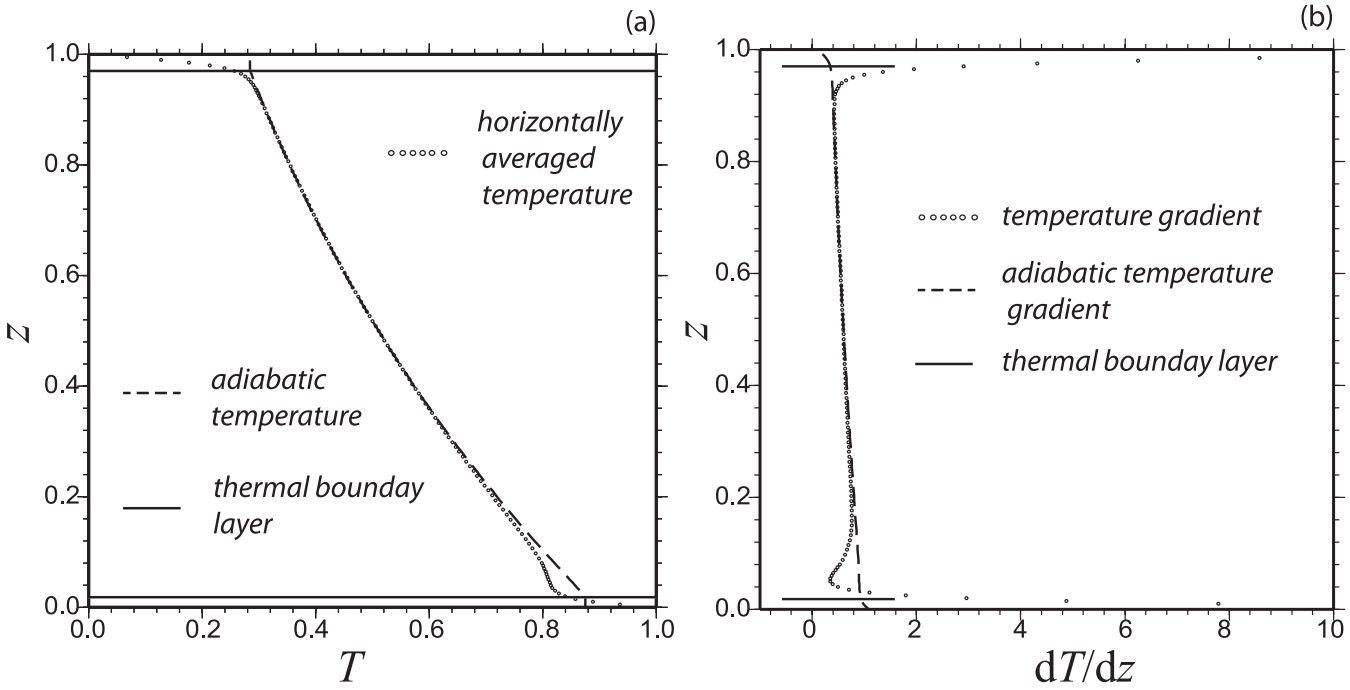

Figure B1. (a) Horizontally averaged temperature profile for case AC1017, with $Di = 1.0$ and $Ra = 10^7$. (b) Temperature gradients for case AC1017. In both (a) and (b), the dotted lines are the horizontally averaged temperature (gradient), where dots show the grid points in the numerical models. The dashed lines are the adiabatic temperature (gradient) (eq. 35). The solid lines in both figures show the TBLs determined by the method introduced in Appendix B.